Draft v0.3.1

CEPC Reference Detector

Technical Design Report

Version: 0.3.1 build: 2025-06-11 13:54:07+08:00

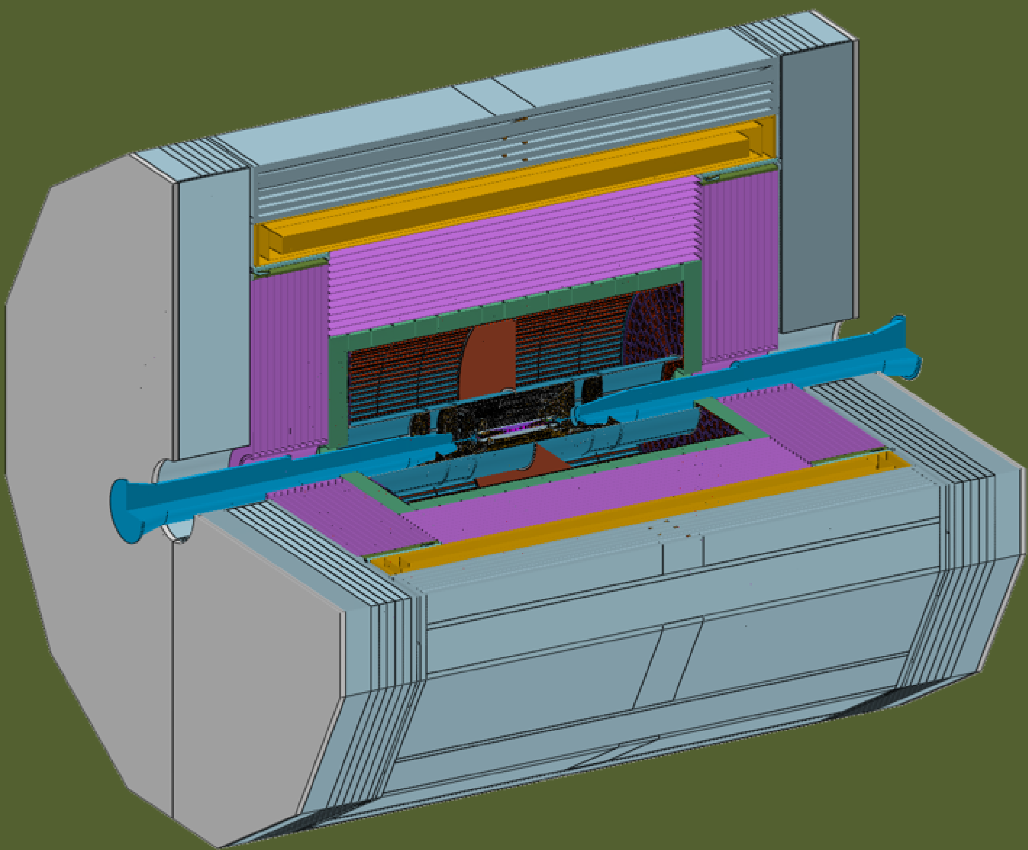

Contents

Chapter 15 Detector and physics performance

The overall performance of the CEPC reference detector is established using a detailed GEANT4 model [1] and full reconstruction of the simulated events. Most of the sub-detectors have been designed with a detailed engineering considerations, including mechanical support structures, electronics, cabling, as well as dead material and cracks. The material budget associated with the support structures and services is based on the best current estimates from the detector R&D groups. Using full simulation and a realistic reconstruction helps ensure that the performance is as realistic as possible and takes into account the detailed knowledge of detector mechanics, dead areas, and non-perfect response. All events are reconstructed using a sophisticated reconstruction chain, with a Kalman-filter based track reconstruction and the CyberPFA particle flow algorithm. A description of the detector parameters and the reconstruction software can be found in the Chapter **??**.

In this chapter, the performance of physics objects from the reference detector is discussed in Section 15.1. Then, a series of different physics studies done using full Monte Carlo at different center of mass energies from 91 to 360 GeV are presented in Section 15.2. These analyses have not been selected to demonstrate the physics reach at CEPC, but rather to stress the detector and its performance. Section 15.3 outlines the strategies for measuring absolute luminosity, the use of resonant depolarization to measure the Z and W masses with high precision, methods for the calibration and alignment for CEPC sub detectors, and the primary areas where detector configuration optimizations and technology decisions could be further explored. Section 15.4 provides a brief summary of the key performance metrics achieved with the reference detector.

15.1 Detector performance

To assess the efficacy of the reference detector and the associated reconstruction software, an in-depth examination of the performance metrics for tracking, Particle Identification (PID), vertexing, and particle flow algorithms has been conducted.

15.1.1 Tracking

The tracking system of the reference detector is designed around three subsystems capable of standalone tracking: the vertex detector (VTX), the inner silicon tracker (ITK) and the time projection chamber (TPC). These are augmented by an auxiliary tracking system, the outer tracker (OTK), which utilizes the AC-LGAD and provides both additional high-resolution measurement points and time of flight information. The TPC provides full coverage down to $\theta \approx 32°$, beyond which the number of measurement points decreases. The final measurement point provided by the TPC is at $\theta \approx 11.7°$. The central inner tracking system, comprising the six-layer VTX and the three-layer ITK, offers nine precise measurements down to $\theta \approx 32°$. The ITK endcap supplies up to a maximum of four measurement points for tracks at small polar angles. The OTK provides a single high-precision measurement point with a large lever arm outside the TPC volume down to a $\theta \approx 8.1°$.

15.1.1.1 Tracking efficiency

With numerous continuous readout layers, pattern recognition and track reconstruction in a TPC is generally efficient, even in environments with significant background noise. Moreover, the standalone tracking capabilities provided by the VTX and ITK allow for the reconstruction of low transverse momentum tracks that do not reach the TPC. The ITK's endcap coverage facilitates the reconstruction of tracks to polar angles as low as approximately $\theta \approx 8.1°$.

Figure 15.1 shows the track reconstruction efficiency as a function of momentum and polar angle for simulated high-multiplicity $ZH \to 4$ jets at a center-of-mass energy of $\sqrt{s}$ = 240 GeV. Efficiencies are calculated relative to Monte Carlo tracks originating within a 10 cm region around the IP, with transverse momentum p_{T} greater than 100 MeV and cos(θ) less than 0.99. This excludes decays in flight and requires at least 90% purity. On average, the combined tracking system achieves a track reconstruction efficiency of 99.7% for tracks with momenta greater than 1 GeV across the full polar angle range. In the region where cos(θ) is less than 0.05, efficiency decreases due to the membrane cathode situated between two rings at the TPC's center.

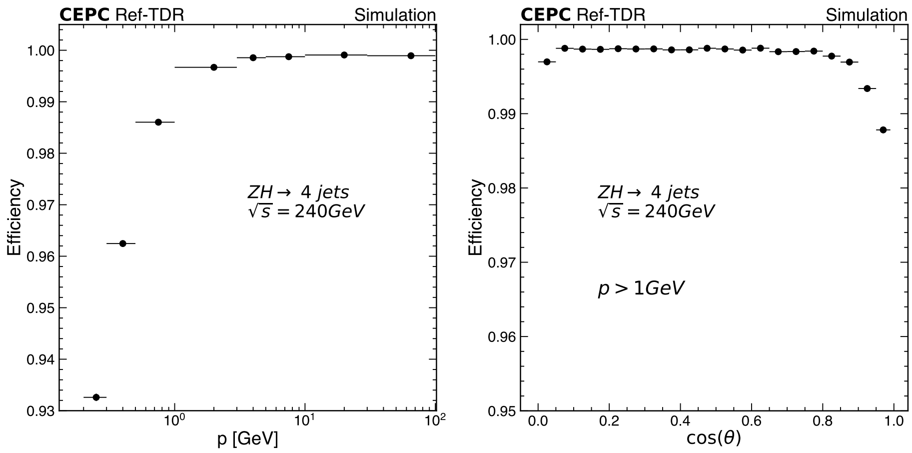

Figure 15.1: Track efficiency as a function of (left) the track momentum and (right) track cos(θ) in the sample of $ZH \to 4$ jets at 240 GeV.

Figure 15.2 shows the track efficiency in the low momentum region for the process

$ZH \to 4$ jets at 240 GeV. The efficiency is presented as a function of either momentum (left) or transverse momentum (right) and cos(θ).

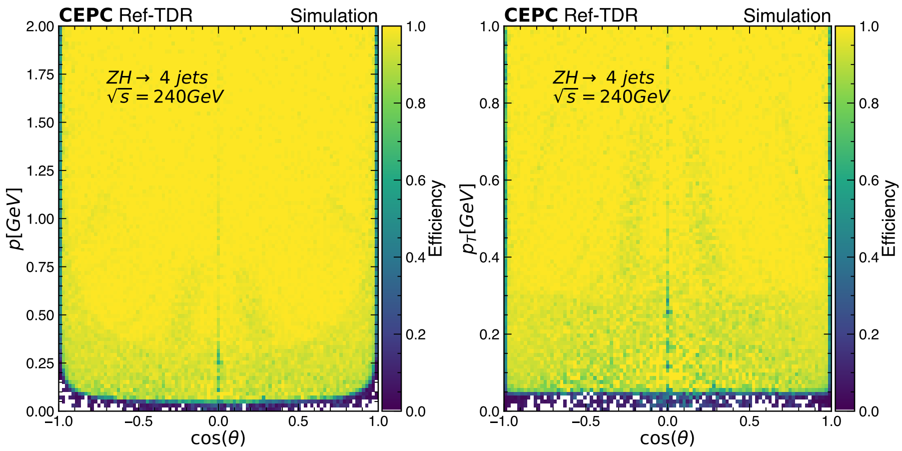

Figure 15.2: Track efficiency in the low momentum region for $ZH \to 4$ jets at 240 GeV plotted against 2D plane of momentum (left) or transverse momentum (right) vs. cos(θ).

15.1.1.2 Momentum resolution

Figure 15.3 left shows track momentum resolutions across various configurations of the tracking system: TPC, VTX+ITK, VTX+ITK+OTK, VTX+ITK+TPC, and VTX+ITK+TPC+OTK. The TPC significantly enhances resolution in the low momentum region. In combination with the OTK, they provides the longest possible radial lever arm for the track fit, improving the resolution at the high momentum region.

The momentum resolutions with the full tracking system at different polar angles are shown in Figure 15.3 right. The study was conducted with muons generated at fixed polar angles of $\theta = 20°, 40°$ and $85°$, with momentum varying from 1 to 100 GeV. For a polar angle of $85°$, this is compared with the parametric form of $\sigma_{1/p_{\mathrm{T}}} = a \oplus b/(p \cdot \sin^{3/2}\theta)$, with $a = 2.9 \times 10^{-5}$ GeV^{-1} and $b = 1.2 \times 10^{-3}$. For high momentum tracks, the asymptotic value of the momentum resolution is $\sigma_{1/p_{\mathrm{T}}} = 3 \times 10^{-5}$ GeV^{-1}. In the forward region, the momentum resolution is inevitably worse due to the relatively small angle between the B-field and the track momentum.

15.1.1.3 Impact parameter resolution

The performance of track's impact parameters is detailed in Section **??**. For $r-\phi$ impact parameter resolution, the required performance is achieved for tracks with momentum down to 1 GeV, while it exceeds expectations for high momentum tracks where the asymptotic resolution is close to 2 μm. The z impact parameter resolution is

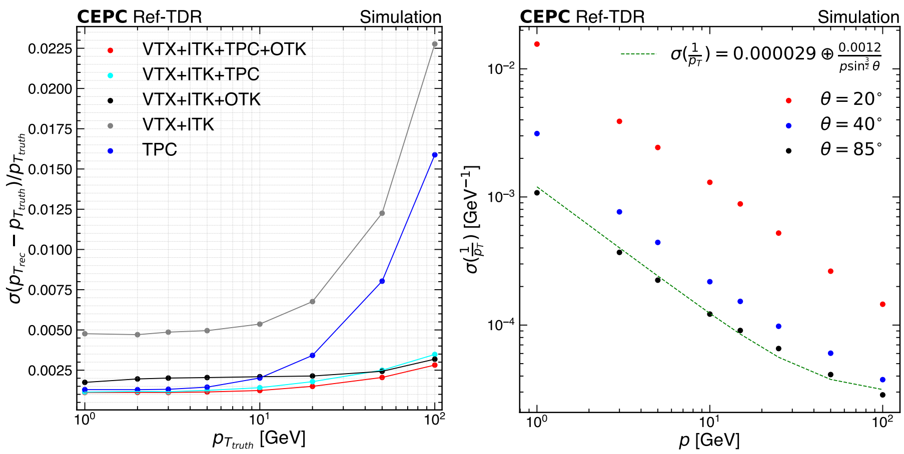

Figure 15.3: (Left) Track resolution for different configurations of the tracking system at the polar angle of $85°$. (Right) Transverse momentum resolution for single muon events as a function of the transverse momentum for different polar angles. The line shows $\sigma_{1/p_{\rm T}} = 2.9 \times 10^{-5} \oplus 1.2 \times 10^{-3}/(p \cdot \sin^{3/2}\theta)$.

similar to the $r - \phi$ resolution and reaches an asymptotic value of ≤ 3 µm for the whole barrel region.

The effects of beam-induced background events and electronics noise have been evaluated and found to be negligible on all the aforementioned tracking performances.

15.1.2 Leptons

The reference detector designed with a focus on particle flow, particularly its highly segmented calorimetry system, provides a wealth of data crucial for identifying leptons. High-energy electrons and hadrons are expected to generate a substantial number of hits, while muons contribute minimally to the calorimeter's energy readings. Electrons can be distinguished by their characteristic, narrow electromagnetic shower patterns in the crystal ECAL, which correlate with tracks detected in the tracking system. In contrast, muons are recognized as particles with minimal ionization in the calorimeter, confirmed by matching their tracks with those in both the tracker and the muon detector.

An eXtreme Gradient Boosting (XGBoost) classifier [2] has been developed to identify muons and electrons against charged hadrons, combining information from different sub-detectors. The following is a list of input variables:

- energy deposit measurements in both calorimeters, divided by the momentum measured in the tracker;
- averaged position of the clusters in both calorimeters weighted by energies;
- Moliere radius of clusters in both calorimeters;
- η and ϕ variances of cluster hits in both calorimeters;
- number of hadronic clusters involved in the PFO;
- number of muon hits matched to the PFO;

- ΔR between the extrapolated track and hits in the muon detectors;
- measurements of dN/dx in TPC;
- time-of-flight measurement in OTK.

The dN/dx and time-of-flight can offer additional means to differentiate between electrons, muons, and hadrons by identifying their different masses. More explanation of these two variables is given in Section 15.1.4.

The XGBoost models are trained and tested with the $ee \to ZH$ samples, in bins of the PFO momentum and θ. The model outputs the probabilities for each PFO to be a muon, electron or hadron. Different working points (WPs) are provided:

- WPs with a fixed efficiency, including 50%, 70%, 90% and 98%. WPs for muons and electrons can be set separately. Muons are identified first: if the PFO has a probability to be a muon higher than the muon WP, it is identified as a muon; otherwise, check if its probability to be an electron is higher than the electron WP; otherwise, it is regarded as a charged hadron.
- BEST WP, the optimal working point, which identifies the PFO as the flavor that it has the highest probability.

The performance metrics for the BEST WP are illustrated in Figure 15.4. In the context of muon identification, the efficiency falls below 50% for momenta less than 2 GeV; notably, the efficiency in the endcap region is lower compared to that in the barrel region. However, as the momentum surpasses 2 GeV, the efficiency rises significantly, reaching levels above 90% and approaching 100%. The rate of misidentification for electrons and charged hadrons is predominantly around 0.1% or lower, demonstrating the system's excellent discriminative capabilities. Similar behaviors can be observed in electron identification, although the misidentification rate for charged hadrons can be higher, peaking at approximately 1% at high momenta. The purity of both electron and muon identifications is predominantly above 90%, indicating a high level of accuracy in the identification process.

As an initial lepton ID approach, further optimizations are anticipated. These will occur alongside the development of improved event reconstruction algorithms, which include the electron tracking algorithm using Gaussian sum filters, enhanced clustering algorithms of energy deposits in the HCAL, and standalone muon track reconstruction in the muon detector.

15.1.3 Photons

Photons have similar signatures as electrons in the calorimeter, but generally do not have matching tracks in the tracker. However, 6–10% of photons in the central region and $\sim$25% of photons in the forward region convert to e^+e^- pairs through their interaction with the materials in front of the calorimeter. Some of these converted photons may have

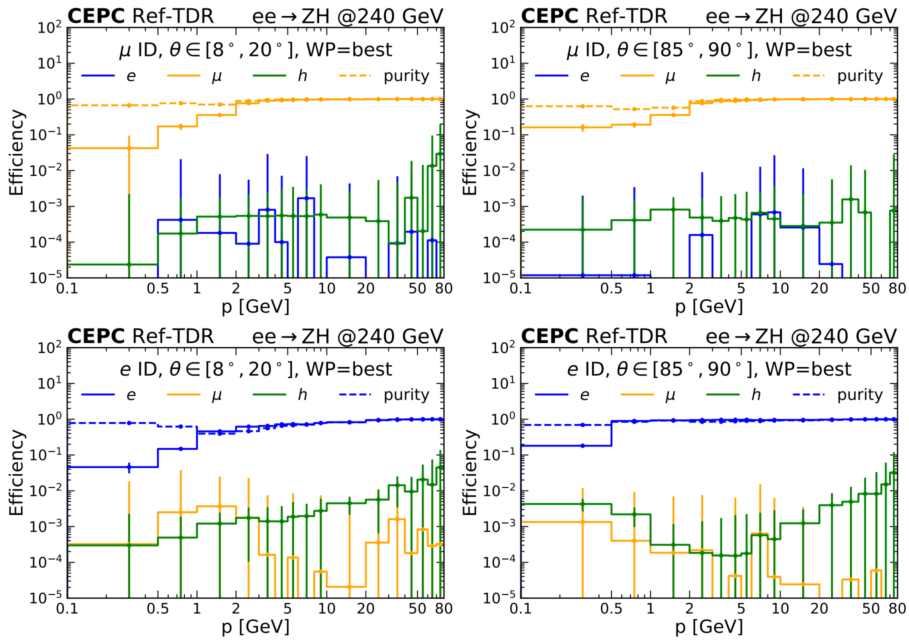

Figure 15.4: The ID efficiency, purity, and misidentification rates with the BEST WP as a function of particle momentum, obtained with the XGBoost models. The top row shows the muon ID; the bottom row shows the electron ID. The left column shows results with $\theta \in [8, 20]^\circ$ in the endcap region; the right column shows results with $\theta \in [85, 90]^\circ$ in the barrel region. Results are computed with full simulation samples of $ee \to ZH$, combining all decay modes of Z and H. In the plots, "h" represents "charged hadron".

reconstructed matching tracks. Figure 15.5(left) shows the amount of material in units of radiation length, and Figure 15.5(right) shows the photon conversion rates at different polar angles.

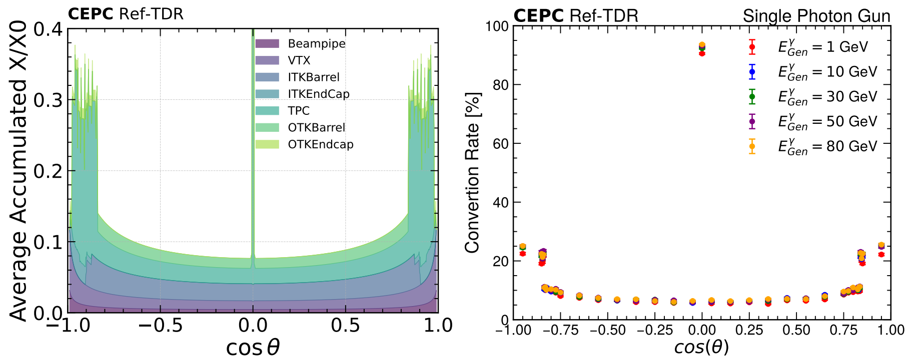

Figure 15.5: (Left) The amount of material in the unit of radiation length inside the tracker and (right) the conversion rate of photons with different energies as function of polar angles.

For unconverted photons, their performance on the reconstruction efficiency and energy resolution is described in Section ??. For photons with energy above 3 GeV, the reconstruction efficiency reaches 100%. Because of the very small stochastic term inherent to homogeneous calorimeters, the photon energy resolution is excellent in the

1–100 GeV range, and reaches well into the sub-percent level for high energy photons.

Unconverted photons need to be distinguished from neutral hadrons, which are predominantly K^0_{L} in the e^+e^- collision environment. Similar to lepton identification, an XGBoost-based algorithm is exploited, using similar input features as those given in Section 15.1.2, except for those from the tracker and muon detectors. The XGBoost models are trained in bins of particle momentum and θ using single-particle samples of photons and K^0_{L}. Particles with a probability higher than 0.5 of being a photon are regarded as photons.

Examples of photon PID efficiency and K^0_{L} misidentification rate are shown in Figure 15.6. The photon ID efficiency remains stable above 90% and approaching 100%. The K^0_{L} misidentification rate is around 2% at $p < 10$ GeV, and around 1% at $p > 10$ GeV. No major difference is observed between the performances in the barrel region and the endcap region.

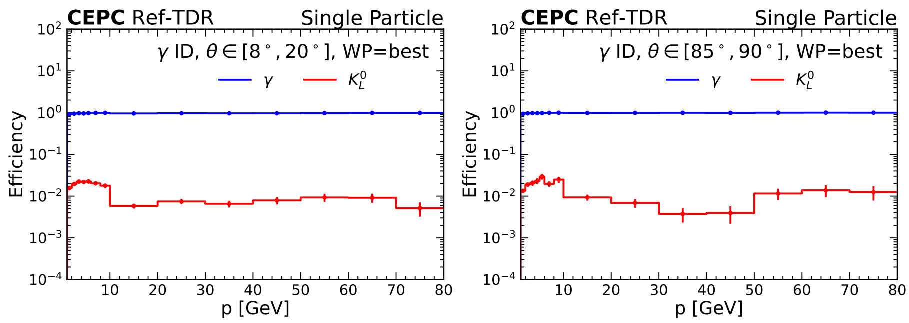

Figure 15.6: The photon ID efficiency K^0_{L} misidentification rate as a function of particle momentum with $\theta \in [8, 20]^\circ$ in the endcap region (left) and $\theta \in [85, 90]^\circ$ in the barrel region (right).

15.1.4 Charged hadrons

Measuring the energy loss of charged particles in the TPC is a powerful tool for identifying particle types. Compared to the energy loss method (dE/dx), the cluster counting method (dN/dx) provides better particle identification by reducing statistical fluctuations in the charge of secondary ionization. The reconstruction algorithm of dN/dx and its separation powers for π, K and p can be seen in **??**.

Additionally, the time-of-flight (TOF) measurement improves identification, particularly in the low-momentum region around 1 GeV. The improvement achieved by combining dN/dx with the TOF measurement is shown in Section **??**.

Using $Z \to q\bar{q}$ events, the performance of kaon identification is evaluated. Figure 15.7 (left) presents the momentum distributions of π, K and p particles. Figure 15.7 (right) illustrates the identification efficiency of charged kaons as a function of momentum and

$|\cos(\theta)|$ based on the χ^2_{Combined}. With $Z \to q\bar{q}$ sample, the kaon identification efficiency and purity can reach 91% and 86.7%, respectively.

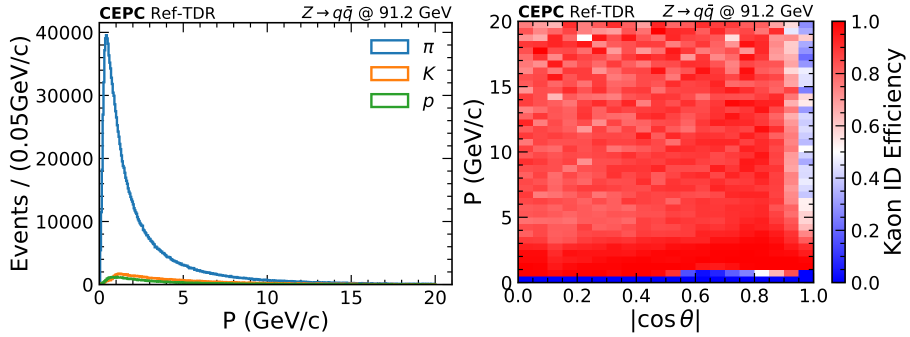

Figure 15.7: (Left) Truth momentum distributions of particles π, K and p after requiring no decay in the $Z \to q\bar{q}$ sample. (Right) Kaon efficiency in $Z \to q\bar{q}$ events is shown as a function of momentum and $|\cos(\theta)|$.

Similar to lepton identification, XGBoost models are trained using categories of particle momentum and θ, utilizing only the TOF and dN/dx data. The overall kaon efficiency is improved to around 92%, and the purity is increased to approximately 90.7%.

15.1.5 Tau leptons

Tau leptons, being the heaviest of the leptons, play a distinctive role in Higgs boson physics research. The leptonic decays of tau leptons, such as $\tau \to e\nu$ and $\tau \to \mu\nu$, are not distinguishable from those of electrons or muons. Hadronic decays of tau leptons appear in the detector as narrow, pencil-like jets with a low multiplicity of particles. An initial τ-lepton identification algorithm has been devised for hadronic decays. This algorithm begins with a seed track whose energy exceeds 1.5 GeV, and gathers charged and neutral particles within a small cone of 0.12 radians to form the τ-lepton candidate. The invariant mass of the particles within this cone must fall within the range of 0.01–2 GeV, aligning with the τ-lepton mass. Additionally, a discriminant variable based on the longitudinal and transverse impact parameters of the leading track is constructed, and this variable must be consistent with the non-zero lifetime of the τ-lepton. Lastly, the τ-lepton candidate must be isolated, with the total energy within an annular cone of 0.12–0.31 radians being less than 8% of the τ-lepton candidate's energy. The primary background consists of hadronic jets, which are significant as they can mimic the signal. The efficiency and purity as functions of the visible energy of the τ-lepton candidate are depicted in Figure 15.8, measured from $e^+e^- \to ZH$ events with $Z \to q\bar{q}$ and $H \to \tau^+\tau^-$ decays. For visible energy between 10–100 GeV, the efficiency approaches 80%, and the purity surpasses 90%. The efficiency loss is largely attributed to the sizeable cone size used for the isolation requirement. Further optimizations are anticipated to enhance performance.

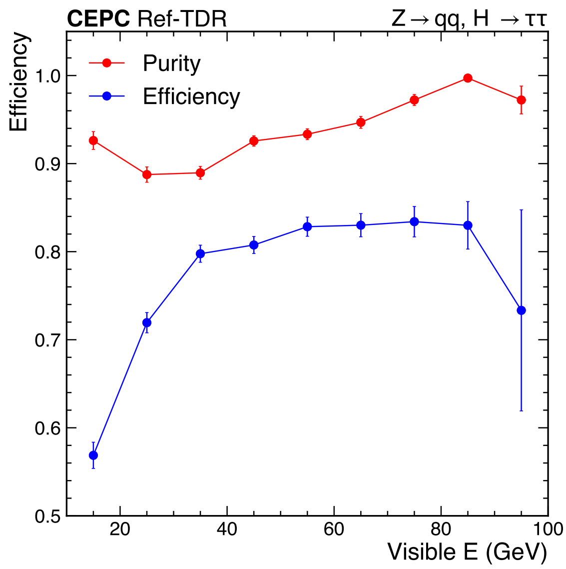

Figure 15.8: The efficiency and purity as functions of the visible energies of the τ-lepton candidates. Both the efficiency and purity are determined from $e^+e^- \to ZH \to q\bar{q}\tau^+\tau^-$ events at $\sqrt{s}$ = 240 GeV.

15.1.6 Vertexing

Vertexing plays a crucial role in event reconstruction by identifying the points where particles originate and decay. Following LCFIPlus[3], a similar algorithm has been developed for this task.

15.1.6.1 Vertex efficiency

In flavor physics, identifying mesons like B or D from a complex track environment near the interaction point is challenging. Accurately resolving secondary vertices helps suppress combinatorial background and enhance signal purity. The performance benchmark for flavor physics 15.2.7 demonstrates how effectively the vertexing algorithm can distinguish signal decays from random track combinations.

For particles with a relatively longer lifetime, they can travel through the tracker volume before decaying, often producing displaced vertices that serve as key signatures. Efficiency in this context is evaluated using $K_S^0 \to \pi^+\pi^-$ events. The efficiency is about 70% and is presented as a function of the particle's flight distance in Figure 15.9 (left).

Unlike the exclusive reconstruction in the aforementioned vertexing implementations, inclusive reconstruction must be performed without any well-defined characteristics of the target events. The algorithm examines all track pairs, discards false candidates based on vertex fitting, and then attempts to attach previously discarded tracks to vertex candidates. This procedure iterates until no more tracks can be connected to the vertex candidates while meeting specific selection criteria. These criteria include the collinearity between the candidate's position vector and the total momentum of all associated tracks, as well as constraints on the energy and invariant mass of the tracks linked to the vertex. Due to the complexity of the vertex and track scenarios in a jet, defining the efficiency of inclusive vertex reconstruction is challenging. To simplify, a true secondary vertex is considered reconstructed if it is found within 200 μm of a reconstructed secondary vertex. Additionally, if a true vertex has more than two tracks, at least two corresponding reconstructed tracks must be used to form this reconstructed secondary vertex. The efficiency for $e^+e^- \to b\bar{b}$ events is 75% and varies with the number of tracks associated with the vertex, as shown in Figure 15.9 (right).

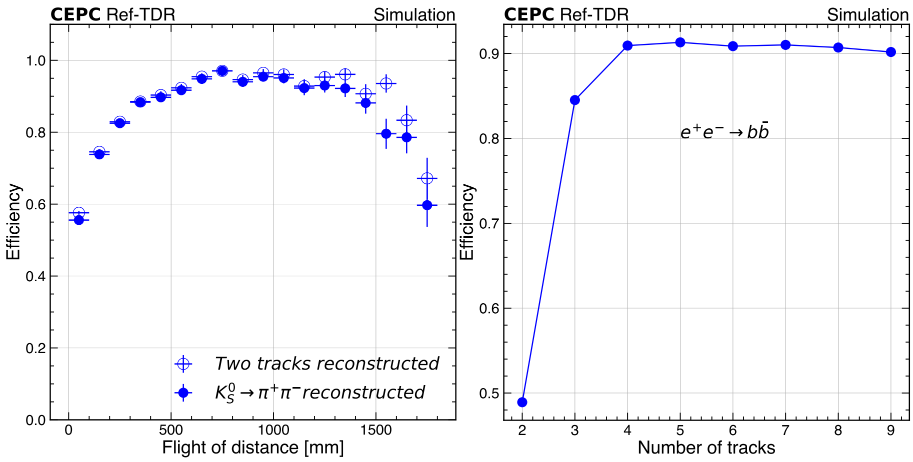

Figure 15.9: (Left) Reconstruction efficiency of $K_S^0 \to \pi^+\pi^-$ as a function of the K_S^0's flight distance; (Right) Reconstructed efficiency of secondary vertex as a function of the number of tracks associated with the vertex in the $e^+e^- \to b\bar{b}$ events.

15.1.6.2 Vertex resolution

The vertex resolution has been assessed using the ZH samples. Figure 15.10 (left) shows the position of the reconstructed primary vertex in the events containing two isolated leptons and two b quarks. The physics interaction has been simulated at the position (0, 0, 0).

Figure 15.10 (right) shows the resolution of the primary vertex position versus the number of tracks originating from the primary interaction. The resolution is better than 3 μm for low multiplicity events and approaches 2 μm for high multiplicity events.

The precision of the secondary vertex is studied using $e^+e^- \to b\bar{b}$ events. It is examined along its orientation to reduce the impact of disturbances caused by boosted events, as represented in the Cartesian coordinate system. This approach clearly demonstrates the vertexing performance. The orientation is derived from the following equation:

$$\vec{e_L} = \frac{\vec{r}}{|\vec{r}|},\ \vec{e_{T1}} = \vec{r} \times \vec{z},\ \vec{e_{T2}} = \vec{e_L} \times \vec{e_{T2}} \tag{15.1}$$

Here $\vec{e_{T1}}$ and $\vec{e_{T2}}$ represent the transverse directions and $\vec{e_L}$ is the longitudinal direction. $\vec{r}$ is the location vector of the corresponding truth vertex and $\vec{z}$ is the beam direction. The

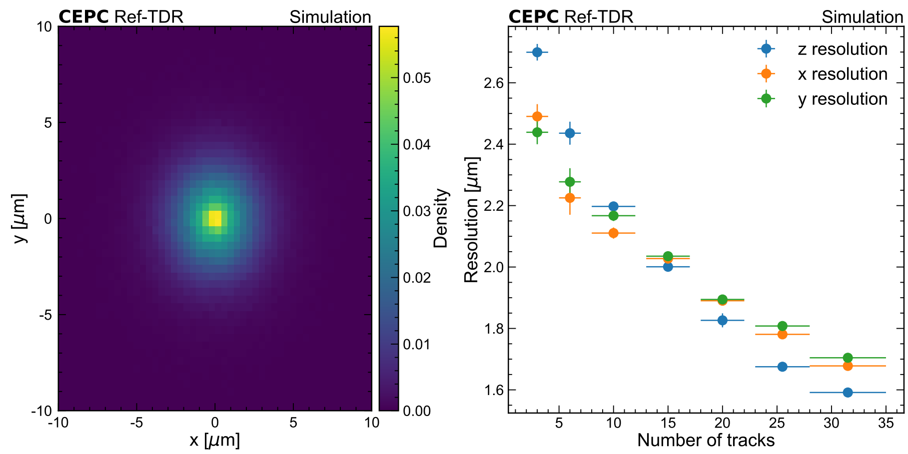

Figure 15.10: Position of the reconstructed primary vertex (left) and resolution of the primary vertex position as a function of the number of tracks originating from that vertex (right).

precision improves as more tracks are associated, as shown in Figure 15.11.

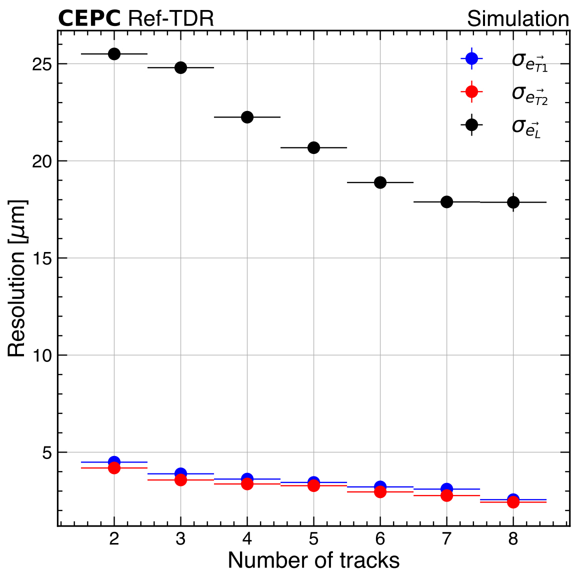

Figure 15.11: Resolution of the transverse and longitudinal components of the secondary vertices as a function of the number of associated tracks.

The overall performance of the reference detector in vertexing is excellent, which was already expected based on the single track impact parameter resolutions.

15.1.7 Jets

The design of the reference detector has been optimized for jet energy resolution using the particle flow approach, which requires a strong interplay among various sub-detectors. This optimization has led to the choice of calorimeters with a high degree of segmentation and transverse granularity. To achieve a jet energy resolution that allows for separation of

W and Z decays, sophisticated reconstruction algorithms are necessary.

The ee-kt algorithm, also known as Durham algorithm [4], is employed as the baseline jet clustering algorithm using the FastJet package [5]. "GenJets" are the clustered truth-level Monte Carlo particles produced from the hadronization of partons simulated by Pythia [6], including subsequent decay products such as photons, leptons, or other lighter hadrons. Neutrinos are excluded from the clustering due to their non-interacting nature, which does not contribute to the energy measurements. "RecoJets" are clustered from the reconstructed final-state particles using the ee-kt algorithm in the same manner as "GenJets", allowing for a comparison of the clustering process at different levels.

15.1.7.1 Jet energy and angular resolution

The jet reconstruction performance of ZH events at $\sqrt{s} = 240$ GeV is analyzed.

The GenJet and RecoJet are matched by minimizing the sum of angles between each pairs. For a given pair, the relative difference is expressed in terms of the jet energy resolution (JER), and the jet angular resolution (JAR). The relative energy difference is modelled with the double-sided crystal ball (DSCB) function, while the angular (polar and azimuth angle) differences of the GenJet-RecoJet pairs are modelled with the Gaussian function. The JER is extracted from the standard deviation (σ) of the DSCB fit to the relative energy difference between RecoJet and GenJet, and the JAR is the σ of the Gaussian fit to the angular difference.

Figure 15.12 shows the differential jet energy resolution as functions of the cosθ_{Gen}, azimuth angle and GenJet energy of the $ZH \to \nu\nu bb$ events. The JER ranges from 4.5% to 6% in the barrel region, and improves as the energy increases, reaching 4.5% for jets with energy greater than 90 GeV , as shown in Figure 15.12 right. The JER is slightly worse in the endcap region, as shown in Figure 15.12 left.

Figure 15.13 and 15.14 show the differential jet angular resolution on polar and azimuthal angles separately, as functions of the cosθ_{Gen}, azimuth angle and GenJet energy of the $ZH \to \nu\nu bb$ events. The JAR is around 0.01 radian for ϕ, and 0.012 radian for θ.

15.1.7.2 Boson mass resolution

Figure 15.15 shows the invariant mass distribution of the Higgs boson in the $ZH \to \nu\nu gg$ sample. When both jets are selected in the barrel region ($|\cos\theta_{\text{jet}}| < 0.85$), the Higgs boson mass resolution (BMR) reaches 3.87%, which is better than the design goal (4%). In the endcap region, the BMR is approximately 6%.

Figure 15.16 shows a clear separation between the W, Z, and Higgs bosons with hadronic final states in their reconstructed invariant mass spectrum.

With further development of the particle flow algorithm, including the integration of PID information, reducing the confusion of photons through π^0 identification, correcting

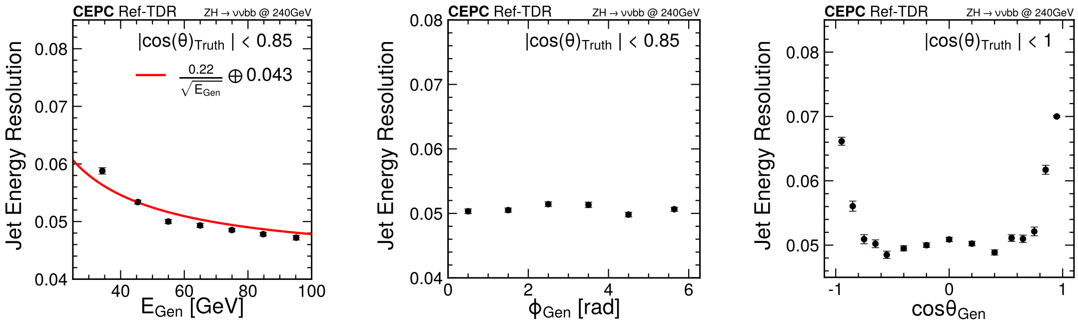

Figure 15.12: Jet energy resolution as functions of the cos$\theta_{\rm Gen}$ (left), the azimuth angle (middle), and the GenJet energy (right) for the $ZH \to \nu\nu bb$ process. The errors shown are only statistical.

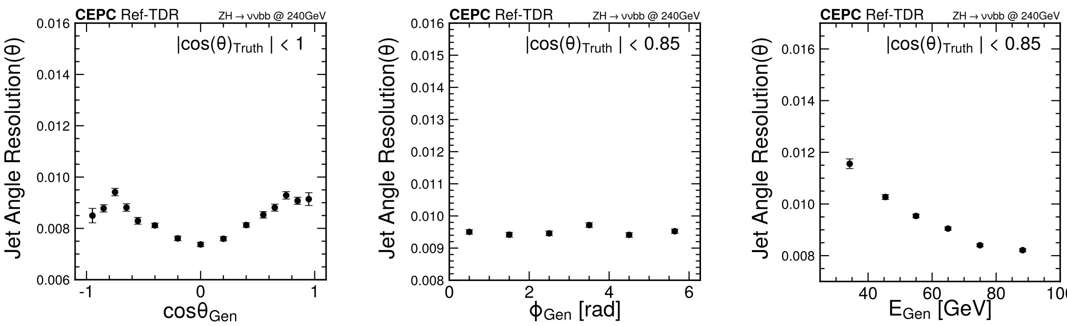

Figure 15.13: $\theta_{\rm jet}$ resolution as functions of the cos$\theta_{\rm Gen}$ (left), the azimuth angle (middle), and the GenJet energy (right) for the $ZH \to \nu\nu bb$ process. The errors shown are only statistical.

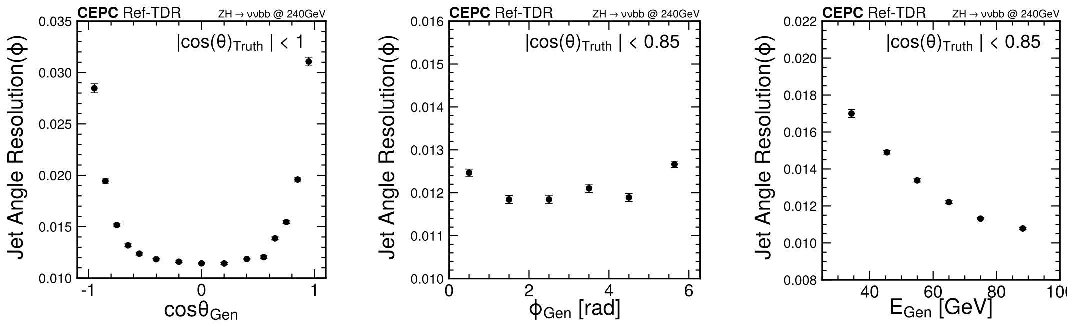

Figure 15.14: $\phi_{\rm jet}$ resolution as functions of the cos$\theta_{\rm Gen}$ (left), the azimuth angle (middle), and the GenJet energy (right) for the $ZH \to \nu\nu bb$ process. The errors shown are only statistical.

neutrino component in the semi-leptonic decays of the heavy flavor jets, etc., the BMR performance is expected to significantly surpass the design goal.

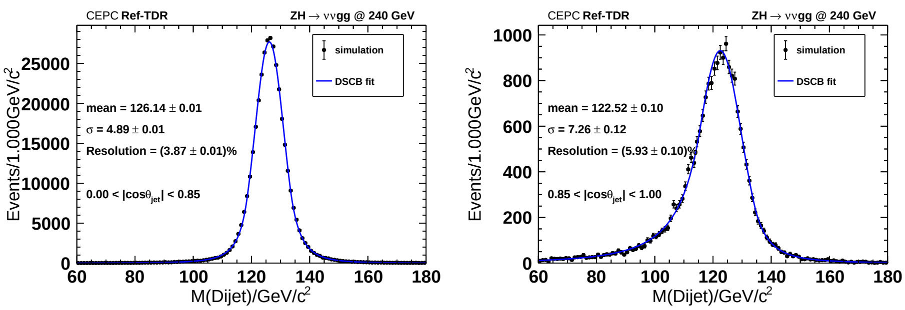

Figure 15.15: Reconstructed di-jet invariant mass distributions in the $ZH \to \nu\nu gg$ process at $\sqrt{s} = 240$ GeV for jets selected in the barrel (left) and endcap (right), separately.

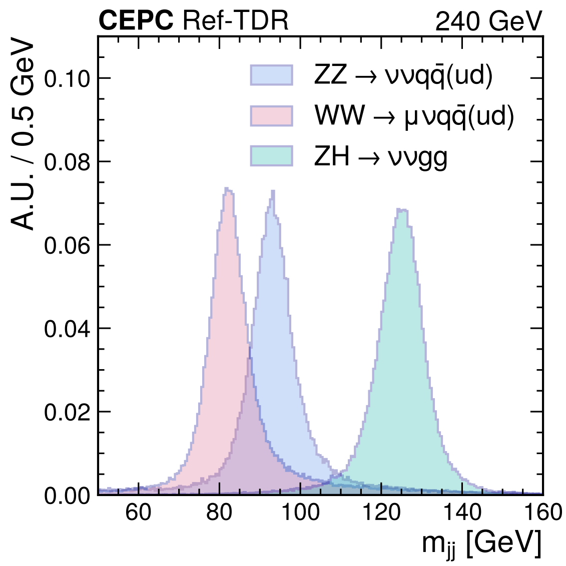

Figure 15.16: Reconstructed di-jet mass distribution from WW, ZZ and ZH processes at $\sqrt{s} = 240$ GeV.

15.1.8 Jet flavor tagging

Identifying bottom, charm, and other quark decay processes is pivotal for assessing the performance of detectors. This capability plays a crucial role in precisely determining the Higgs boson couplings and electroweak observables at CEPC. Two specific approaches have been explored to quantify the tagging performance.

15.1.8.1 Jet flavor tagging with BDT

XGBoost is well-suited for jet flavor tagging, offering both strong classification performance and excellent interpretability, which are essential for understanding the underlying detector performance.

In this study, the XGBoost classifier is set up for three jet categories: b-jet, c-jet and uds-jet. The variables used in the classification are listed in the Table 15.1. The flavor tagging performance in $e^+e^- \to q\bar{q}$ events at $\sqrt{s} = 91.2$ GeV is shown in Figure 15.19, with separate evaluations for b tagging and c tagging. The curves represent misidentification rates for different jet flavors. For b tagging, the misidentification rates at $\epsilon_{b\text{-jet}}$ = 80% (50%) are 2.2% (0.11)% for c-jets and 0.24% (0.03%) for uds-jets. For c tagging, the misidentification rates at $\epsilon_{c\text{-jet}}$ = 80% (50%) are 13.6% (2.9%) for b-jets and 13.9% (0.78%) for uds-jets.

Table 15.1: BDT input variables for jet tagging

Name	**Description**
VtxLxyz	Decay length of the vertex.
VtxLxyzSig	Significance of the decay length (calculated using the covariance matrix).
VtxMomenta	Magnitude of the momenta of all tracks forming the vertex.
VtxEnergy	Sum of the track energies of the vertex.
VtxMass	Mass of the vertex, calculated using the tracks' four-momentum.
VtxAngle	Angle between the vertex position direction and the total track momentum.
VtxCollinearity	Collinearity between vertex position direction and the total track momentum.
VtxNtrk	Number of tracks forming the vertex.
VtxChi2	Chi-square of the vertex fitting.
VtxNumber	The number of vertices reconstructed in the jet.
VtxTotalTrk	Total number of tracks forming all vertices in the jet.
VtxTotalMass	Total mass of all vertices, computed as the sum of all tracks' four-momenta.
VtxDistance	Distance between the first two vertices.
VtxDistanceSig	Significance of the distance between the first two vertices.
SingleVtxProb	Vertex probability with all associated tracks combined.
MultiVtxProb	For multiple vertices, the probability P is computed as $1 - P = (1 - P_1)(1 - P_2)(1 - P_3)\dots$
TrkTotalMass	Total mass of all tracks exceeding 5σ significance in d_0/z_0 values.
TrkTotalD0Prob	Product of the d_0 probabilities of all tracks under the $b/c/uds$-quark hypotheses using the corresponding d_0 distributions.
TrkTotalZ0Prob	Product of the z_0 probabilities of all tracks under the $b/c/uds$-quark hypotheses using the corresponding z_0 distributions.
TrkD0Sig	d_0 significance of the two tracks with the highest d_0 significance.
TrkZ0Sig	z_0 significance of the two tracks with the highest d_0 significance.
TrkPt	Transverse momentum of the two tracks with the highest d_0 significance.

15.1.8.2 Jet Origin Identification

Jet Origin Identification (JOI) [7] is a novel approach for distinguishing jets originating from different quarks and gluons. It utilizes an advanced artificial intelligence algorithm specifically designed for jet flavor tagging and jet charge measurement. Developed using the GNN-based ParticleTransformer framework, JOI enables the simultaneous identification of 11 distinct jet species—five quarks, five anti-quarks, and gluons—at the proposed electron-positron Higgs factory.

To evaluate JOI performance, we fully simulate $\nu\bar{\nu}H$ production with $H \to u\bar{u}$, $d\bar{d}$, $s\bar{s}$, $c\bar{c}$, $b\bar{b}$, and gg at a center-of-mass energy of 240 GeV, employing the reference detector. For each process, one million physics events are generated, with 800,000 used for training, 100,000 for validation, and 100,000 for testing. The reconstructed final-state particles are clustered into two jets using the eek_t algorithm. For each jet, kinematic and particle species information—including track impact parameters for charged particles, and particle identification described in 15.1.2 is fed into the ParticleTransformer algorithm. The comprehensive set of input variables is listed in Table 15.2.

The algorithm computes likelihoods for classification into 11 jet categories and assigns each jet to the type with the maximum likelihood value. The model is trained for 30 epochs, and the epoch yielding the highest accuracy on the validation sample is selected for application to the test dataset to extract the final numerical results.

Table 15.2: Input variables used in the ParticleTransformer algorithm for jet flavor tagging at the CEPC, including kinematic and particle-specific features.

Variable	**Definition**
p_x, p_y, p_z, E	particle 4-momentum, with energy E derived from PID.
$\Delta\eta$	difference in pseudorapidity between the particle and the jet axis
$\Delta\phi$	difference in azimuthal angle between the particle and the jet axis
$\log p_{\mathrm{T}}$	logarithm of the particle's p_{T}
$\log E$	logarithm of the particle's energy
$\log \frac{p_{\mathrm{T}}}{p_{\mathrm{T}}(\text{jet})}$	logarithm of the particle's p_{T} relative to the jet p_{T}
$\log \frac{E}{E(\text{jet})}$	logarithm of the particle's energy relative to the jet energy
ΔR	angular separation between the particle and the jet axis
d_0	transverse impact parameter of the track
$d_0$err	uncertainty associated with the measurement of the d_0
z_0	longitudinal impact parameter of the track
$z_0$err	uncertainty associated with the measurement of the z_0
charge	electric charge of the particle
PID	Reconstructed particle type of $e, \mu, \pi, k, p, \gamma$ and neutral hadron

Figure 15.17 shows the JOI performance via an 11-dimensional confusion matrix M_{11}, with jets classified by their highest likelihood category.

Overall, the matrix exhibits approximate quark-anti-quark symmetry and can be block-diagonalized into 2×2 submatrices, each corresponding to a specific quark species. This confusion matrix provides a comprehensive assessment of the model's classification performance, highlighting both accurate and misclassified predictions across various jet categories.

To further quantify JOI performance, we evaluate three distinct scenarios shown in Figure 15.18: (1) perfect PID, (2) realistic PID reconstruction, and (3) charged tracks

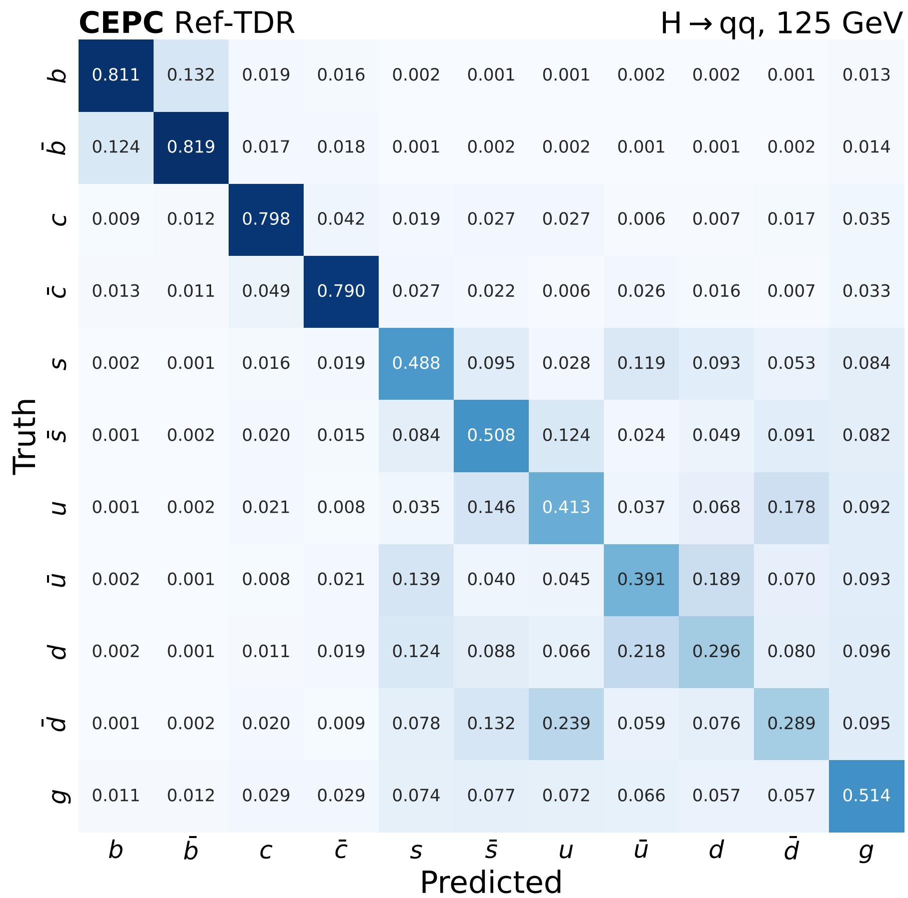

Figure 15.17: The confusion matrix M_{11} with reconstructed identifications of $e^{\pm}, \mu^{\pm}, \pi^{\pm}, K^{\pm}, p^{\pm}$ for $\nu\bar{\nu}H$, $H \to qq$ events at $\sqrt{s} = 240$ GeV, with the reference detector. The matrix is normalized to unity for each truth label.

only (excluding neutral components). While the realistic PID scenario shows slightly degraded performance compared to the ideal case - primarily due to lost PID information for low-energy tracks - the b- and c-jet tagging efficiencies remain stable as their vertex information (d_0 and z_0) provides strong discrimination power. The charged-track-only analysis demonstrates that while neutral particle exclusion reduces performance, which reflects the impact of electromagnetic calorimeter, the JOI remains functional, confirming the robustness of the algorithm even with partial detector information.

Compared to the conceptual detector, the reference detector achieves moderate improvement in JOI performance, mostly owing to the calorimeter redesign that enhances energy reconstruction.

Compared to the XGBoost method described in the previous section, the jet tagging efficiency versus the misidentification fraction for b, c, uds, jet, and the comparison to XGBoost method is shown in Figure 15.19. Generally, JOI performance is about one order of magnitude better compared to the BDT method. This localized performance inversion at low b-jet efficiencies is likely an artifact of data sparsity and statistical fluctuations in a rarely optimized or statistically robust region of the ROC curve, rather than true superiority. Remarkably, current JOI achieves a b-jet tagging efficiency of 95% with a misidentification rate of only 0.1% for light quark jets.

This JOI model, optimized within a Higgs-boson production environment, demonstrates sufficient universality and generalization capability across diverse kinematic energy scales. Critically, its application to $Z \to qq$ final states reveals no significant performance degradation when compared against JOI models specifically tailored for $Z \to qq$ data. Furthermore, the model's consistent performance is validated for $ee \to qq$ jet samples at different center-of-mass energies, specifically for 240 and 360 GeV, highlighting its energy-independent robustness beyond the training environment.

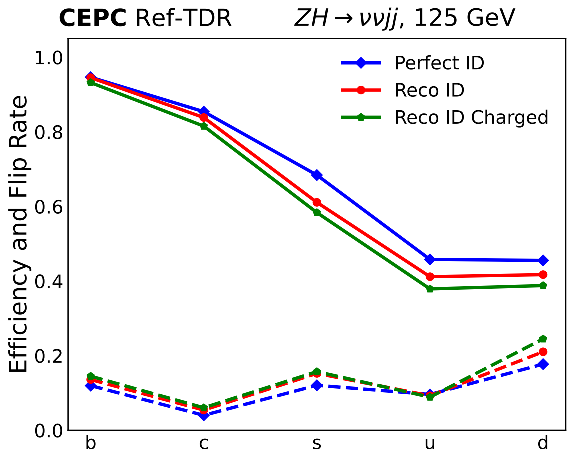

Figure 15.18: Comparison of JOI performance under three conditions: perfect PID, realistic PID reconstruction, and realistic PID reconstruction using only charged tracks.

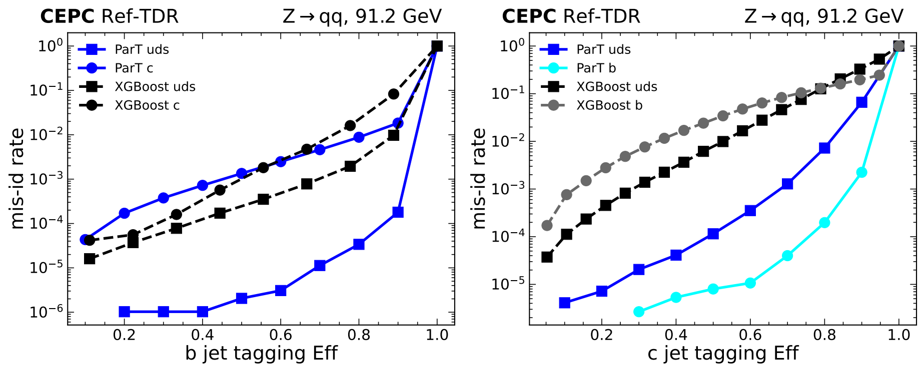

Figure 15.19: Jet tagging efficiency versus mis-identification rate for b-tagging (left) and c-tagging (right). Solid for JOI with ParticleTransformer, dashed for XGBoost, solid circle point for mis-id rate from heavy quarks (c or b jets), solid square for mis-id rate from light quarks (uds).

15.1.9 Missing energy, momentum, mass

Neutrinos interact with detectors through weak interactions and evade detection, leaving no discernible traces. This characteristic is also attributed to hypothetical dark matter particles. Nevertheless, the presence of these elusive particles can be deduced from observable particles and plays a crucial role in the CEPC physics program. Approximately 20% of Z bosons and 30% of W bosons decay into final states that include neutrinos. The pursuit of Higgs boson decays into dark matter particles represents a pivotal objective of the Higgs factory. Reconstruction of the missing energy, momentum or mass can also show the detector coverage capacity and the overall performance of the particle flow algorithm to reconstruct all flavors of particles.

At the CEPC reference detector, thanks to its excellent energy and momentum resolution, large coverage of the solid angle, and full knowledge of the initial state, the missing energy and momentum can be determined with high precision. The Higgs boson invisible decay at $\sqrt{s} = 240$ GeV is used to illustrate the performance. The Higgs strahlung production is considered, with $Z \to \mu\mu, ee$ or qq, and $H \to ZZ^* \to 4\nu$. Additionally, the Higgs strahlung production with $Z \to \nu\nu$ and $H \to qq$ is also considered. The distributions of the reconstructed missing mass are shown in Figure 15.20. For $H \to 4\nu$, the missing mass distributions are always around 125 GeV, while for $Z \to \nu\nu$, they are around 91 GeV. The missing mass is fitted with double-sided crystal ball functions in each channel. The $Z \to \mu\mu$ has the best missing mass resolution of 0.288 GeV, while the ee channel gives a slightly worse resolution of 0.40 GeV because the tracking for electrons is more complicated due to their higher energy loss in the tracker and higher rate of final state radiations. In the qq channels, light quarks give the best resolution, which is around 6.4 GeV for $Z \to$ light quarks, $H \to 4\nu$ and 9.2 GeV for $Z \to \nu\nu, H \to gg$.

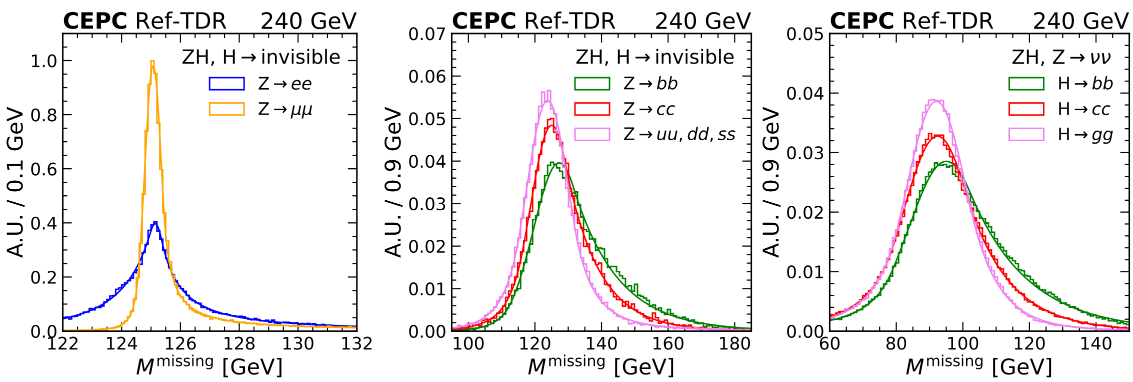

Figure 15.20: The distributions of reconstructed missing mass in the ZH production, with $Z \to ee/\mu\mu, H \to 4\nu$ (left), $Z \to qq, H \to 4\nu$ (middle) or $Z \to \nu\nu, H \to qq$ (right). The solid lines show the fitted double crystal ball functions. In the middle and right plots, different quark flavors are drawn and fitted separately.

15.2 Physics benchmarks

Results of detailed simulation studies of the reference detector are discussed in this section. Benchmark studies were conducted at various center-of-mass energies of 91 GeV, 240 GeV, and 360 GeV, as shown in Table 15.3. These studies cover essential physics areas such as Higgs, electroweak, flavor, top, and new physics. For each benchmark, the most relevant sub-detectors are highlighted.

Table 15.3: Physics Benchmarks and Relevant Detector Performances

Physics Benchmarks	Process @ c.m.e	Domain	Relevant Det. Performance
$H \to \gamma\gamma$	ZH @ 240 GeV	Higgs	photon ID, EM resolution
Recoil Hmass	$\mu\mu H$ @ 240 GeV	Higgs	Tracking
$H \to$ hadronic decays	ZH @ 240 GeV	Higgs	PID, Vertexing, PFA (+ JOI)
$H \to$ invisible	$\mu\mu H$ and qqH @ 240 GeV	Higgs/NP	PFA, MET, BMR
$H \to$ LLP	ZH @ 240 GeV	NP	Tracker, Calo, muon detectors
Smuon pair	@ 240 GeV	NP	Tracking
W fusion Xsec	$\nu\nu H$ @ 360 GeV	Higgs	PFA, b-tagging
Top mass & width	Threshold scan @ $\sim$ 345 GeV	Top	Beam energy
A^{μ}_{FB}	$e^+e^- \to \mu^+\mu^-$ @ 91.2 GeV	EW	Tracking, muon ID
R_b	$Z \to$ hadronic @ 91.2 GeV	EW	PFA + JOI
CPV in $D^0 \to \pi^+\pi^-\pi^0$	@ 91.2 GeV	Flavor	PID, vertex, π^0, EM resolution

15.2.1 Event Generation

The production of events for the benchmarking analyses includes the generation of a comprehensive set of the SM processes. The mass of the SM Higgs boson is set to 125 GeV.

The benchmarking studies primarily use the WHIZARD1.9.5[8] event generator for cross-section calculations and Monte Carlo sample generation. Hadronic fragmentation is simulated using Pythia6.3 [9]. At the CEPC, Higgs signal production mechanisms manifest through three principal channels: Higgsstrahlung ($e^+e^- \to ZH$), W-boson fusion ($e^+e^- \to \nu\nu H$), and Z-boson fusion ($e^+e^- \to e^-e^-H$).

The background processes, excluding Higgs signals, can be broadly classified into two major categories based on the number of final-state particles:

- $e^+e^- \to$ 2-fermion processes, encompassing leptonic pair production (e.g., e^+e^-, $\mu^+\mu^-$, $\tau^+\tau^-$, ...) and quark-antiquark generation (e.g., $q\bar{q}$)
- $e^+e^- \to$ 4-fermion processes, which exhibit significant complexity, necessitating a detailed treatment of electroweak interference effects. These 4-fermion backgrounds are systematically categorized by their intermediate bosonic contributions:
  - WW production ($e^+e^- \to W^+W^- \to 4f$)
  - ZZ production ($e^+e^- \to ZZ \to 4f$)
  - Single W production ($e^+e^- \to We\nu$)

- Single Z production ($e^+e^- \to Zee$)

The comprehensive analysis of cross-sections for all aforementioned processes is systematically presented in Table 15.4.

Notably, the WHIZARD generator demonstrates particular efficacy in handling gauge boson production processes, interference effects, and initial state radiation correction, which are critical for precision measurements at CEPC energies.

For photon related processes, the WHIZARD generator automatically manages the initiated and final state photons by default. For example, final states such as $e^+e^- \to q\bar{q}\gamma\gamma$ are included in $e^+e^- \to q\bar{q}$ process, with an invariant mass and energy cut of 10 GeVfor photon emission. Similarly, the process $e^+e^- \to e^+e^-e^+e^-$ considers the effect from diphoton pair production contribution with the same cut.

4-fermion samples are categorized into 40 individual types, ensuring no overlap or omission during the generation. Without overlap and disregarding the interference, the overall 4-fermion cross section at 240 GeVis 19.3 pb, and at 360 GeV, the overall corss section is 14.7 pb. For 6-fermion process other than $t\bar{t}$, such as ZW or ZZ processes, the cross section is estimated to be smaller than 20 fb and is not recorded in the table.

Then the events go through full simulation and reconstruction chain in CEPCSW. The detailed information on the samples produced, including their statistics and data paths, is maintained in a centralized database using the GitLab service provided by IHEP.

15.2.2 Higgs mass measurement through recoil mass

Since the discovery of the Higgs boson at the LHC in 2012 [12, 13], extensive efforts have been made to accurately measure its mass. The most precise measurement of m_H to date is m_H = 125.11 $\pm$ 0.11 GeV [14], obtained by the ATLAS experiment. The projected precision at HL-LHC is 30-50 MeV, depending on different performance assumptions by the ATLAS and CMS experiments. These measurements rely on specific Higgs decays, where the signals are either limited by low event yields or affected by significant hadronic backgrounds and pileup in the hadron collider environment.

At CEPC, the Higgs bosons are primarily produced through the Higgs-strahlung process $e^+e^- \to ZH$ with a cross-section of 200 fb at $\sqrt{s} = 240$ GeV. This study aims to report the expected precision of m_H measurement using the $e^+e^- \to ZH \to \mu^+\mu^-X$ events, where X represents inclusive final states. Due to the well-known initial state particles and beam energy, this method requires only the measurements of the two muons from Z-boson decay, which recoil against the Higgs boson, making the result independent of the Higgs boson's decay modes. This study is crucial for validating the detector design and assessing its expected sensitivity, particularly in terms of tracking efficiency, momentum resolution, and muon identification in the relevant momentum range.

Signal events are characterized by two oppositely charged, high-momentum muons.

Table 15.4: Cross sections for Higgs production and background processes at $\sqrt{s} = 240$ GeV and 360 GeV. Note that there are interference between the same final states from different processes after the W or Z boson decays, see text. With the exception of the Bhabha process, the cross sections are calculated using the Whizard [8]. The Bhabha cross section is calculated using the BABAYAGA event generator [10] requiring final-state particles to have $|\cos\theta| < 0.99$. The $t\bar{t}$ process are generated by qqbarthreshold [11] generator. Photons, if any, are required to have $E_\gamma > 0.1$ GeV and $|\cos\theta_{e^\pm\gamma}| < 0.99$. ISR and FSR effects are included in all the final states.

Process	Cross section @ 240 GeV	Cross section @ 360 GeV
Higgs boson production, cross section in fb		
$e^+e^- \to ZH$	196.9	126.6
$e^+e^- \to \nu_e\bar{\nu}_e H$	6.2	29.6
$e^+e^- \to e^+e^- H$	0.5	2.8
Total Higgs	**203.6**	**159.0**
background processes, cross section in pb		
$e^+e^- \to e^+e^-(\gamma)$ (Bhabha)	930	325
$e^+e^- \to q\bar{q}(\gamma)$	54.1	23.2
$e^+e^- \to \mu^+\mu^-(\gamma)$	5.30	2.1
$e^+e^- \to \tau^+\tau^-(\gamma)$	4.75	–
$e^+e^- \to t\bar{t}$	–	0.566
$e^+e^- \to WW$	16.7	11.3
$e^+e^- \to ZZ$	1.1	0.68
$e^+e^- \to e^+e^- Z$	4.54	5.83
$e^+e^- \to e^+\nu W^- +$ c.c.	5.09	6.04

As discussed in Section 15.1.1, within the detector acceptance, these muons are expected to be efficiently captured and reconstructed with a transverse momentum precision better than 0.3%. A signal muon pair forms a Z boson with an invariant mass close to m_Z = 91.19 GeV, while the remaining part of a Higgsstrahlung event consists of the decay products of the Higgs. The recoil mass of the muon pair can be calculated using the beam energy according to Equation 15.2, without requiring explicit knowledge of the Higgs decay components. The recoil mass spectra are shown in Figure 15.21.

$$M_{\text{rec}}^2 = (\sqrt{s} - E_{\mu^-} - E_{\mu^+})^2 - |\vec{p}_{\mu^-} + \vec{p}_{\mu^+}|^2 \tag{15.2}$$

To achieve high purity and efficiency in detecting signal events, specific criteria are applied to the kinematic variables of the muons. Muons originating from Z decay are expected to have a momentum close to 45 GeV. To select these muons, both lower and upper momentum thresholds are set. To suppress soft muons originating from jets or other resonances in ZH events, a minimum momentum threshold of 20 GeV is enforced. Additionally, in $e^+e^- \to \mu^+\mu^-$ events, muons typically exhibit higher momentum. Therefore, an upper limit of 80 GeV is also applied to enhance the selection's overall purity.

For the event-level requirements, it is essential to select any events resembling a Z boson, meaning the invariant mass of the di-muon final state must be within the range of 50-120 GeV. At the same time, taking into account the phase space of the ZH process, the momentum of the Z boson should be constrained to avoid being excessively high. Therefore, the momentum of the di-muon system is limited to the range of 20-60 GeV.

Noticing that the $e^+e^- \to \mu^+\mu^-$ background process has a significantly larger cross-section than both the signal process and other backgrounds, the primary focus of background suppression needs to be effectively reducing its contribution. Most muons from this background possess nearly half of the center-of-mass energy, so imposing an upper limit of 110 GeV on the di-muon energy can serve as a criterion for rejecting these events. Furthermore, muons from $e^+e^- \to \mu^+\mu^-$ background with ISR may have lower energy and could contribute to the Z peak. To suppress such events, a variable for undetected momentum in the beam direction called MEZ, is introduced. If MEZ exceeds 50 GeV, it is likely that an ISR photon has been emitted in the final state. By applying these selection criteria, this background can be effectively suppressed across nearly the full energy range. The event selection criteria are summarized in Table 15.5, in which the four-fermion backgrounds are categorized as their final states.

Table 15.5: Summary of event selections and cutflow. Four-fermion backgrounds are categorized by their final states

Final States	$2\nu2\mu$	4μ	$2\ell\,2q$	2μ	$\mu\mu H$
Events number	120000	40000	80000	100000	40000
Muon pair	31.43%	41.70%	29.52%	88.21%	95.58%
$M_{\text{rec}} \in [110, 150]$ GeV	5.83%	8.46%	3.39%	42.04%	88.19%
MEZ $\in [0, 50]$ GeV	4.68%	5.85%	3.02%	25.78%	87.10%
$E_{\mu\mu} \in [0, 110]$ GeV	4.05%	5.13%	2.99%	25.28%	86.58%
$p_{\mu\mu} \in [20, 60]$ GeV	2.67%	3.43%	2.15%	6.49%	78.73%
$m_{\mu\mu} \in [50, 120]$ GeV	2.64%	3.15%	1.74%	6.48%	78.71%

After event selections, the shape of the signal M_{rec} is modeled using double-sided Crystal Ball function. Ideally, the peak position parameter of this function equals m_H . The background is modeled using a Chebyshev polynomial, which is obtained by fitting the background-only M_{rec} distribution and is fixed in the signal-plus-background model. The spectra within the signal region 110-150 GeV and the signal-plus-background shape are shown in Figure 15.21.

The expected precision of m_H is estimated by extrapolating the statistics from simulated signal and background events to their expected yields at an integrated luminosity of 20 ab^{-1}. The statistical uncertainty is $\Delta m_H = \pm 3.1$ MeV.

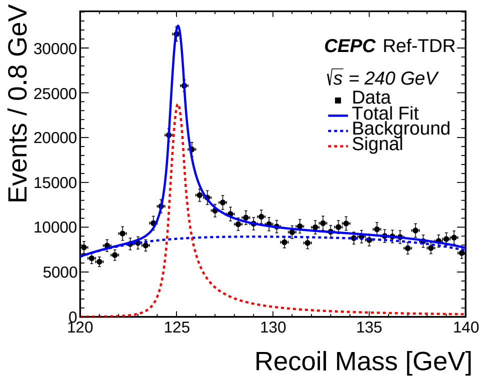

Figure 15.21: M_{rec} distribution and the models for signal and background. The beam energy spread has been included.

Some foreseeable systematic uncertainties are considered.

- Momentum scale: $3 \times 10^{\ 7}$ radiative return events with $\mu\mu\gamma$ as final state will be generated at $\sqrt{s}$=240 GeV. This process serves as a standard candle for precision measurements, benefiting from very large statistics. With a tracking resolution of 0.2%, it allows monitoring of the Z peak shift with a relative precision at the level of 10^{-6}. Considering that the limiting factors may include the magnetic field and the tracker alignment algorithm, the uncertainty of momentum scale is assumed to be 2 MeV.
- Center-of-mass energy: The uncertainty in center-of-mass energy directly propagates into the Higgs recoil mass spectrum, as shown in Equation 15.2. It can be monitored using $e^+e^- \to f\bar{f}\gamma$ events, with precise knowledge of the Z boson mass and excellent understanding of tracking. For this analysis, it is assumed to be 2 MeV.
- Beam energy spread: Beam energy spread is expected to be 0.17% at $\sqrt{s}$=240 GeV and has been included in the signal modelling. Its uncertainty can be measured using the radiative return events, achieving a precision of 1%. This effects on m_H is studied using a perturbed sample and is found to be negligible.
- Initial state radiation: Initial state radiation can alter the Higgs recoil mass spectrum by reducing the effective collision energy. As a theoretical uncertainty in QED, it is not considered difficult to handle. For conservatism, the impact on m_H is assumed to be 1 MeV.
- Beam-induced background: After mixing beam-induced background with signal events, the recoil mass spectrum of $e^+e^- \to \mu^+\mu^- HX$ is found to be 5 MeV wider than before. To account for the beam-background effects temporarily, a nuisance parameter of 5 MeV is added to the width parameter in the signal model. Its contribution to Δm_H is negligible.

These systematic uncertainties contribute an additional 3.7 MeV to Δm_H, resulting in a final precision Δm_H=± 4.8 MeV. This result can be further improved by combining it with the electron channel, making the CEPC experiment's target precision for the Higgs mass measurement achievable.

15.2.3 Branching ratios of the Higgs boson in hadronic final states

According to theoretical predictions, the branching fractions for the decay of a 125 GeV Higgs boson into $b\bar{b}$, $c\bar{c}$, gg, $\tau\bar{\tau}$, WW^*, ZZ^* are 57.7%, 2.91%, 8.57%, 6.32%, 21.5% and 2.64%, respectively. The measurements can be conducted simultaneously together with full hadronic decay modes of WW^*/ZZ^* and the backgrounds from processes with two-fermion and four-fermion final states. The ParticleTransformer(ParT) is employed for the multi-classification of those different decay modes.

Currently, only Higgs production via ZH process with Z decaying to a pair of muons is considered. Each event must contain at least two oppositely charged tracks, reconstructed as a muon pair. In cases where more than two muons are selected, the muon pair with the invariant mass closest to the Z boson mass is chosen as the Z candidate, corresponding to a Z-mass window of 75 GeV to 105 GeV. The invariant mass of the recoil system, must fall within the Higgs mass window of 110 GeV to 150 GeV. To further reduce the two-fermion background, the polar angle of muon pair system is required to be in the range of $|\cos\theta_{\mu\mu}|$ <0.996.

Table 15.6 and 15.7 presents the event selection efficiencies for various signal and background processes, detailing the efficiency at each selection step relative to the previous requirement. In addition, the total efficiency is defined as the ratio of the number of events satisfying all selection criteria to the total number of events expected from the process considered (signal or background). For signal processes, a high efficiency of over 80% is observed. In contrast, two-fermion background processes exhibit a total efficiency of around 0.3%, four-fermion backgrounds have total efficiencies of 0-3%, while other backgrounds are found to be negligible.

Table 15.6: The cutflow selection efficiency for signal processes.

Process	$b\bar{b}$	$c\bar{c}$	gg	$\tau\bar{\tau}$	WW^*	ZZ^*	$s\bar{s}$
Muon pair	93.4%	93.1%	92.9%	94.3%	93.0%	93.1%	93.2%
Isolation	93.0%	93.3%	93.7%	94.6%	93.6%	93.8%	93.5%
Z mass window	96.1%	96.1%	96.1%	93.2%	96.0%	96.0%	96.0%
Hmass window	99.6%	99.6%	99.6%	98.5%	99.6%	99.6%	99.6%
$\|\cos\theta_{\mu\mu}\|$ <0.996	99.6%	99.7%	99.6%	99.7%	99.6%	99.7%	99.7%
Total eff.	82.8%	82.9%	83.0%	81.6%	82.9%	83.2%	83.0%

Based on the thirteen classification task, there are thirteen reconstructed categories, the migration matrix M_{mig} is defined as the probability $\epsilon_{i,j}$ of genuine signal with class i reconstructed as category j as shown in Figure 15.22, and can be unfolded for the

Table 15.7: The cutflow selection efficiency for background processes.

Process	$(ZZ)_l$	$(ZZ)_{sl}$	$(WW)_l$	ll	$(SZ)_l$	$(mix)_l$
Muon pair	46.1%	18.8%	11.0%	11.9%	9.7%	29.3%
Isolation	77.4%	68.8%	98.0%	94.6%	48.2%	96.1%
Z mass window	66.4%	70.4%	34.7%	41.8%	28.3%	16.8%
H mass window	15.6%	16.3%	58.6%	6.6%	29.3%	41.1%
$\lvert\cos\theta_{\mu\mu}\rvert$ <0.996	98.8%	99.5%	98.7%	90.3%	99.0%	99.4%
Total eff.	3.7%	1.5%	2.2%	0.3%	0.4%	1.9%

branching fraction measurements. The migration matrix reflects the overall high accuracy of the model.

Figure 15.22: The migration matrix for the 13 classes is shown. The horizontal axis represents the prediction of the model for each event in the test set, while the vertical axis indicates the true labels. The sum of values in each row equals to 1.

By considering all signal and background processes, the numbers of expected events for each process can be calculated as in the following:

$$\begin{bmatrix} N_{S1} \\ N_{S2} \\ \cdots \\ N_{B1} \\ N_{B2} \\ \cdots \end{bmatrix} = (M_{\text{mig}}^T M_s)^{-1} \times \begin{bmatrix} n_{S1} \\ n_{S2} \\ \cdots \\ n_{B1} \\ n_{B2} \\ \cdots \end{bmatrix} \tag{15.3}$$

where n_i and N_i are the number of reconstructed events in cateegory i and number of expected events of class i, respectively. The M_s is a diagonal matrix containing the selection efficiencies, while M_{mig}^T denotes the transposed migration matrix.

Based on Higgs production via ZH process with Z decaying to a pair of muons and ParT method, the branching fractions of $H \to b\bar{b}/c\bar{c}/gg/\tau\bar{\tau}/WW^*/ZZ^*/s\bar{s}$ at the CEPC, with a center-of-mass energy of 240 GeVand luminosity of $20ab^{-1}$, are measured to be 57.7%, 2.9%, 8.6%, 6.3%, 21.5%, 2.6% and 0.04%, with the statistical uncertainty of 0.4% , 6.7% , 2.4% , 1.2% , 1.5% , 18.6%, 266.5% respectively. To account for detector response effect, the spatial resolution of each track was adjusted to 10 μm, the corresponding systematic uncertainties for the branching fractions are estimated to be 0.3%, 24.8%, 5.0%, 0.04%, 1.5%, 66.0% and 1636.9%.

Table 15.8: The measured branching fractions for the Higgs decays along with their statistical and systematic uncertainties are shown.

Decay channels	$b\bar{b}$	$c\bar{c}$	gg	$\tau\bar{\tau}$	WW^*	ZZ^*	$s\bar{s}$
Br	57.7%	2.9%	8.6%	6.3%	21.5%	2.6%	0.04%
Stat. Un.	0.4%	6.7%	2.4%	1.2%	1.5%	18.6%	266.5%
Syst. Un	0.3%	24.8%	5.0%	0.04%	1.5%	66.0%	1636.9%

15.2.4 $H \to \gamma\gamma$

The diphoton decay channel of Higgs boson is one important benchmark channel in the future Higgs factory. The branching ratio is small due to the origin involving top quark and massive boson loop, but it has very clean final state with two energetic photons. Regarding the homogeneous ECAL design in this reference detector, an improvement is expected in the precision of $H \to \gamma\gamma$ measurement.

Following the strategy in CDR [15], this analysis focuses on the ZH production at $\sqrt{s}$ = 240 GeV, with Higgs decaying to two photons. Three sub-channels are considered based on Z decays: $Z \to q\bar{q}$, $\mu^+\mu^-$, and $\nu\bar{\nu}$. The $Z \to e^+e^-$ channel is excluded due to overwhelming Bhabha background, and $Z \to \tau^+\tau^-$ is omitted due to the complexity of τ identification. The dominant background ($e^+e^- \to f\bar{f}$) with two ISR/FSR photons is considered, while the others, including the Higgs resonant contributions, four fermion processes and reducible backgrounds from photon mis-identification are expected to be negligible. The events are generated as described in Sec. . The signal samples are generated with full simulation and reconstruction process to have precise detector response, while the background samples are processed through the fast simulation with Delphes for large statistics.

Regarding the kinematic topology of the photons from Higgs boson and fermions from Z boson decay, the events are tagged into 3 channels. Event selection are applied to reject the backgrounds and mis-tagged events. The leading (subleading) photon energy is required to be greater than 30 GeV(20 GeV), and the invariant mass of diphoton needs to be within [110, 140] GeVin all three channels. Additional cuts on the angular and energy of photons, fermions or missing mass are applied individually depending on the final state. The final efficiency and expected yields are listed in Table 15.9. The contamination between three sub-channels are examined to be minor (<0.3%) after the event selection. A gradient boosted decision tree (BDTG) is trained for event categorization to further suppress the background. The distributions in three channels are shown in Figure **??**. The chosen variables keeps the same as in [15]. The criteria of category definition is optimized by scanning the cut value on BDTG for highest signal significance.

Table 15.9

	Selection efficiency	Expected yield at 20 ab^{-1}
$q\bar{q}$yy signal		
$q\bar{q}$yy background		
mmyy signal		
mmyy background		
nnyy signal		
nnyy background		

Table 15.10: Expected precisions on $\sigma(ZH) \times \text{Br}(H \to \gamma\gamma)$ from Asimov data fitting in the three channels (and their combination). The statistical precision includes the contribution from background modeling.

	$\frac{\Delta_{stat}}{(\sigma\times\text{Br})_{SM}}$
$q\bar{q}\gamma\gamma$	0.0403
$\mu^+\mu^-\gamma\gamma$	0.155
$\nu\bar{\nu}\gamma\gamma$	

15.2.5 $H \to$ invisible

In the SM, the Higgs boson can decay to two Z bosons, each decaying to two neutrinos, with a branching ratio of 0.106%. On the other hand, BSM models predict more scenarios of the Higgs boson invisible decays, including those into dark matter, supersymmetric particles, etc. Compared to the LHC and HL-LHC, future electron-positron colliders would provide much improved sensitivities [16–18] thanks to the low background, and full reconstruction of the missing information.

Searches for the Higgs boson invisible decay are performed with full simulation samples at $\sqrt{s} = 240$ GeV, described in Section 15.2.4. For the signal, we consider the Higgs strahlung process, with the Z boson decaying into two muons, two electrons or two quarks; and the Higgs boson decaying into four neutrinos. All background processes are considered, including other Higgs boson production and decay channels, 4-fermion final state and 2-fermion final state processes.

Events firstly pass the baseline selection and are categorized into three channels, selected successively:

- The 2μ channel: events should contain exactly two PFOs passing the BEST muon ID WP and with $|\cos\theta| < 0.99$. The two muons should have the opposite charge, and their invariant mass between 40 and 120 GeV.
- The $2e$ channel: events should satisfy the same criteria as the 2μ channel, except for the lepton ID being replaced to that for the electrons.
- The $2q$ channel: events should not be in the channels above, and should have visible mass between 30 and 130 GeV, and visible momentum between 10 and 80 GeV.

The missing mass M^{miss}, introduced in Section 15.1.9, has the strongest sensitivity to the signal among the kinematic variables considered in the analysis. Its distributions are presented in Figure 15.23 for the three channels. The signal processes are distributed around 125 GeV, whereas backgrounds are broadly distributed with different features depending on their physics processes. Especially, the irreducible backgrounds that have the same final states as the signal, shown as the magenta histograms in each plot, is mainly composed of the ZZ production, and therefore distributed around 91 GeV.

Events are further selected based on M^{miss} as well as other variables, including the number and total energy of the charged or neutral particles, visible energy and momentum, missing energy and momentum. The selection efficiency for the signal and background processes are summarized in Table 15.11.

After event selection, an XGBoost model is trained in each channel to discriminate signal and background processes, exploiting all variables mentioned above, as well as lepton impact parameters and jet substructure variables. The distributions of the output scores are shown in Figure 15.24. Most backgrounds are concentrated around zero. The major backgrounds that have large contamination in the high score region are the

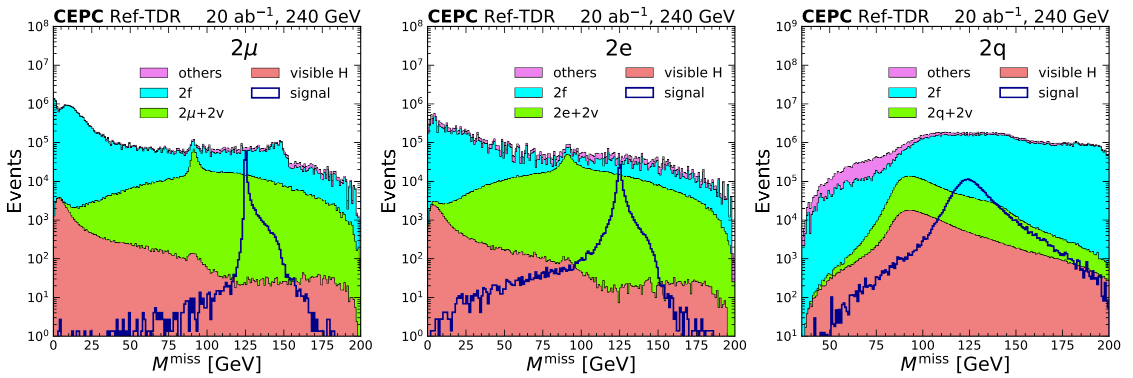

Figure 15.23: The $M^{\rm miss}$ distributions of signal and background processes in the 2μ (left), $2e$ (middle) and $2q$ (right) channels after baseline selection, estimated with simulation samples. For visibility, the invisible decay branching ratio is set to be 1.

Table 15.11: Total generated yields, baseline selection efficiency, further selection efficiency, and selected yields of different signal and background processes, in different channels. For the signal process, only the final state corresponding to the channel is considered.

process		signal	$2(\mu/e/q)$+2v	2-fermion	visible H	others
2μ	total yield	1.44e+02	5.68e+06	1.78e+09	4.07e+06	3.79e+08
	Baseline sel	96.1%	32.0%	2.35%	2.55%	0.88%
	Further sel	98.0%	19.8%	3.40%	0.44%	5.31%
	selected	1.35E+02	3.59E+05	1.42E+06	4.55E+02	1.78E+05
$2e$	total yield	1.49e+02	5.57e+06	1.78e+09	4.07e+06	3.79e+08
	Baseline sel	83.8%	41.7%	1.03%	1.96%	1.60%
	Further sel	95.3%	23.0%	3.35%	2.19%	5.77%
	selected	1.19E+02	5.35E+05	6.13E+05	1.75E+03	3.49E+05
$2q$	total yield	2.90e+03	7.39e+06	1.78e+09	4.07e+06	3.77e+08
	Baseline sel	99.0%	66.1%	9.24%	19.8%	8.35%
	Further sel	95.4%	38.1%	37.3%	37.8%	12.9%
	selected	2.74E+03	1.86E+06	6.13E+07	3.04E+05	4.05E+06

irreducible backgrounds. The distributions of the XGBoost score are directly fitted to perform statistical analyses. Systematic uncertainties including luminosity, beam energy measurements, efficiencies and resolutions are estimated with impacts of less than 1%, negligible compared to statistical uncertainties. For the SM invisible decay, expected uncertainties on the decay branching ratio and statistical significances are computed; for BSM scenarios, the SM signal is added as an additional background, and expected upper limits (UL) at 95% confidence level on the decay branching ratio are computed.

Results are shown in Table 15.12. In general, the $2q$ channel has the highest sensitivity. The combined significance is expected to reach 4.4 σ with 20 ab^{-1}, significantly improved in comparison to Ref. [18], thanks to the multivariate analysis approach.

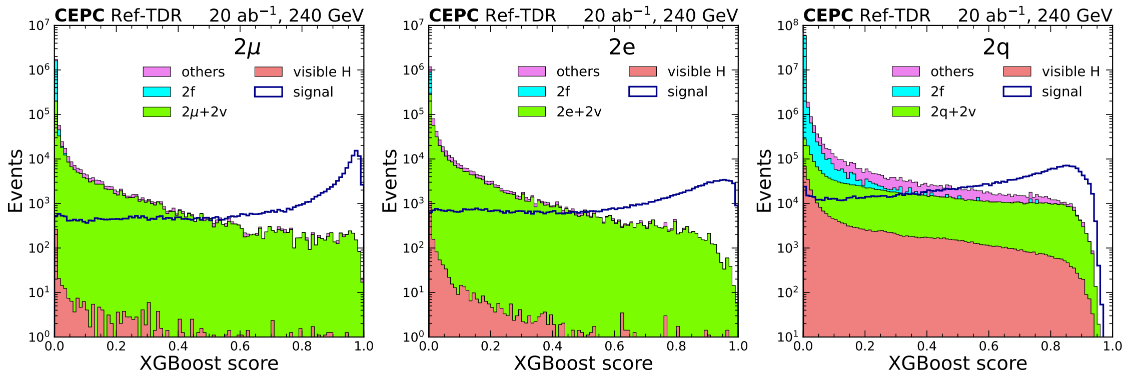

Figure 15.24: The XGBoost score distributions of signal and background processes in the 2μ (left), $2e$ (middle) and $2q$ (right) channels. For visibility, the invisible decay branching ratio is set to be 1.

Table 15.12: Expected relative uncertainties, statistical significance of the SM Higgs boson invisible decay, and upper limits on the BSM invisible decay branching ratio for 20 ab^{-1} in each channel and all channels combined.

channel	uncertainties	significance	UL
2μ	$-43\%/+44\%$	2.4 σ	0.093%
$2e$	$-62\%/+65\%$	1.6 σ	0.14%
$2q$	$-31\%/+31\%$	3.3 σ	0.064%
combine	$-23\%/+23\%$	4.4 σ	0.049%

15.2.6 R_b at Z pole

The measurement of R_b, which represents the relative partial decay width of the Z boson into $b\bar{b}$ final states ($R_b = \frac{\Gamma_{b\bar{b}}}{\Gamma_h}$, where $\Gamma_{b\bar{b}}$ is the partial decay width of $Z \to b\bar{b}$ and Γ_h is the total hadronic decay width), holds paramount significance in the vast landscape of particle physics. It serves as a fundamental cornerstone for testing the Standard Model (SM) and a highly sensitive probe for uncovering new physics phenomena beyond its current framework [19–22].

The current experimental landscape for R_b measurements is shaped by data from experiments conducted at renowned facilities such as the Large Electron - Positron Collider (LEP) and the Stanford Linear Collider (SLC) [23–28].

At the Circular Electron-Positron Collider (CEPC), jets play a pivotal role in the measurement of R_b [29, 30]. Jets are formed when quarks and gluons undergo the process of hadronization, and their properties can be meticulously analyzed to infer the flavor of the originating quark. Jet flavor tagging, therefore, emerges as a crucial technique in this measurement, which can be a key benchmark reflecting the vertex detector performance. In this study, the jet flavor tagging is performed using the advanced tagging algorithm called the JOI tagger. More technical details can be found in Sec. 15.1.8.2. Instead of using the full 11 categories as in the Sec. 15.1.8.2, several categories are merged with

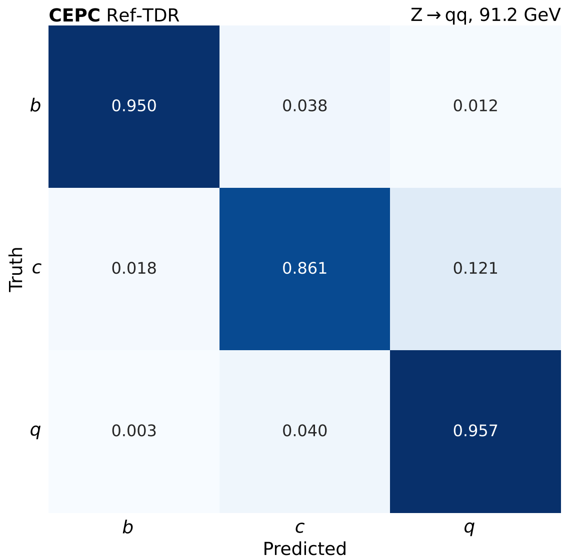

Figure 15.25: The confusion matrix after category merging. This confusion matrix is produced with $Z \to b\bar{b}$, $Z \to c\bar{c}$ and $Z \to q\bar{q}$ (light-quarks) sample generated at $\sqrt{s} = 91.2$ GeV.

the following scheme: quark and anti-quark categories for the same flavor are merged; categories besides b and $c$quark are merged into the light-quark category. With such a merge scheme, a total of 11 categories are reduced to 3 ones.

In this analysis, the criteria used to tag b, c, and q(light-quarks) is the same as Sec.15.1.8.2 to calculate the confusion matrix, thus, the tagging efficiencies could be obtained from a 3-dimensional confusion matrix(M_3). This confusion matrix is calculated from a set of simulated samples corresponding to $Z \to b\bar{b}$, $Z \to c\bar{c}$, $Z \to s\bar{s}$, $Z \to d\bar{d}$, and $Z \to u\bar{u}$ with such the same convention as the original 11-dimensional matrix, where more detail of the convention could be found in Sec.15.1.8.2. Such a matrix is shown in Figure 15.25, and is further used in R_b and R_c measurement.

The measurement of R_b at CEPC is accomplished through the implementation of the double-tagging method. This method is based on a meticulous counting of the number of jets of a particular flavor in two distinct scenarios: single-tagged jets and double-tagged jet pairs. The observed number of single - tagged jets of flavor i ($N_s^{i,obs}$) and double - tagged jet pairs ($N_d^{i,obs}$) are intricately related to R_b, R_c, R_q ($R_q = 1 - R_b - R_c$) and the tagging efficiencies (ε_{ij}) through the following equations [29–31]:

$$N_s^{i,\mathrm{obs}} = 2N^{\mathrm{h,pro}} \cdot (R_b\varepsilon_{ib} + R_c\varepsilon_{ic} + R_q\varepsilon_{iq}) \tag{15.4}$$

$$N_d^{i,\mathrm{obs}} = N^{\mathrm{h,pro}} \cdot \left[R_b\varepsilon_{ib}^2 + R_c\varepsilon_{ic}^2 + R_q\varepsilon_{iq}^2\right] \tag{15.5}$$

Here, $N^{\mathrm{h,pro}}$ is the total number of Z boson hadronic events produced in collisions. These equations form the foundation of the double-tagging method, allowing for a precise determination of R_b based on the measured jet counts and known tagging efficiencies which are obtained from the confusion matrix.

	$\sigma_{R_b}(10^{-6})$	$\sigma_{R_c}(10^{-6})$	$\sigma_{R_q}(10^{-6})$	Flavor tagging method
LEP+SLC	659	3015	–	–
FCCee	2.1	–	–	–
CEPC (template fit)	1.2	2.3	2.1	LCFIPlus
CEPC (PartNet)	1.3	1.4	–	ParticleNet
CEPC (JOI)	1.3	1.5	–	JOI

Table 15.13: Comparision of statistical uncertainties of R_b, R_c, R_q measurement from difference methods.

With the definition above, for each flavor jet (b, c, and q), there are two equations associated, resulting in a total of six equations. These equations are over-determined, meaning there are more equations than unknowns, which can be solved using the least-squares method. To assess the reliability of the R_b measurement, a toy Monte Carlo approach is employed to calculate the statistical uncertainty. In this approach, a large number of Z hadronic decay events (10^{11} in this study) are sampled according to the Poisson distribution. These events are then further sampled into three categories ($b\bar{b}$, $c\bar{c}$, and $q\bar{q}$) according to the multinomial distribution. The statistical uncertainty provides a measure of the reliability of the R_b measurement, indicating the range within which the true value of R_b is likely to lie.

A comparison of statistical uncertainties of R_b and R_c measurement from different experiments and methods is shown in Table 15.13. The results of the R_b and R_c measurements at CEPC demonstrate a significant improvement compared to previous experiments such as LEP/SLC. The double-tag method at CEPC achieves a precision comparable to that of the template fit method [31]. Only statistical uncertainty is evaluated in the current analysis. Both theoretical variations, such as modeling of quark radiation and gluon splitting ($g \to b\bar{b}$), and experimental corrections on track and PFO properties are the main source of systematic uncertainty in the R_b (R_c) measurement. Such uncertainties have a much higher impact compared to statistical uncertainty and need more detailed studies.

15.2.7 CP violation searches in $D^0 \to h^- h^+ \pi^0$

The branching ratio of Z boson decays to a pair of charm and bottom quarks are BR($Z \to c\bar{c}$) $\simeq 12\%$, BR($Z \to b\bar{b}$) $\simeq 15\%$ in the SM, respectively, which suggests that the CEPC Z-pole operation mode could also serve as a charm and bottom factory. A comparison of the expected yields of charm and bottom hadrons from BESIII, Belle-II, LHCb and CEPC Z-pole operation mode is shown in Table 2 in Ref. [32].

The yields of heavy flavour hadrons from CEPC are larger than those from existing electron-positron colliders by one or several orders of magnitudes, and CEPC can also access heavy hadrons that other electron-positron colliders cannot produce. Due to the large production cross-section in hardron collider, LHCb can produce much more heavy flavour hadrons than CEPC, however, the complicated collision environment makes the reconstruction and selection efficiency at LHCb much smaller than CEPC. Therefore, CEPC can remain advantages in many cases, especially for bottom hadron decays, or decays contain neutral particles. Given the CEPC's high luminosity, low background, and excellent detector performance, CEPC may significantly enhance the precision of certain studies in heavy flavour physics.

In order to reconstruct heavy flavour decay events, charged track measurement, vertex reconstruction, particle identification, and neutral particle reconstruction are crucial. Here, we choose to use $D^0 \to h_1^- h_2^+ \pi^0$ (where "$h_{1/2}$" represent either a Kaon or a pion) decays as benchmark decays, to demonstrate the impact of detector performance to flavour physics studies.

CP violation in Charm meson decays was recently discovered by LHCb experiment [33], however, it only discovered in two-body decays. Multi-body decays provides rich resonance structures, which could help us understand the source of CP violation. The sensitivity of CP violation searches largely depend on the sample statistics. Due to the large branching fraction of the singly-Cabibbo-suppressed decay $D^0 \to \pi^-\pi^+\pi^0$, it potentially could be a sensitive channel for studying CP violation in multi-body decays, and the Cabibbo-favoured decay channel $D^0 \to K^-\pi^+\pi^0$ will serve as a reference channel.

In order to get a reasonable estimation of the yields, a quantitative study of the efficiency for reconstructing and selecting D^0 decays has to be proceed. We produced inclusive $Z \to qq$ full simulation sample using CEPCSW. Then from this sample, we could reconstructed two charged tracks that came from a same vertex that displaced from the primary vertex. For $D^0 \to h^-h^+\pi^0$ decays, an additional neutral pion need to be reconstructed using two photon clusters recorded by ECAL, an invariant mass constraint need to be applied to the two charged tracks and the neutral pion. The neutral pions from flavour physics interested decays usually has smaller momentum, therefore the photons from those pions also have relatively low momenta (Figure 15.26 a), and the single photon reconstruction efficiency is relatively low for low energy photons , therefore, in order to suppress background and maintain efficiency, the following strategy were used to reconstruct neutral pions: firstly, using generator level MC sample, the open angle distribution between two photons is obtained (Figure 15.26 b), we choose 10° as the criteria to suppress random combinations. secondly, a photon with energy larger than 0.5 GeV is selected as the leading photon, thirdly, a second photon is searched closed to the leading photon, with energy requirement to be $E > 0.1$ GeV. With this selections, most of the background can be suppressed, while the efficiency can be $\mathcal{O}(0.1)$.

A dedicated PID efficiency study was then performed using dNdx only PID and dNdx+TOF PID information, to estimate the impact of different detector designs to the final efficiency. A preliminary qualitative estimate of several D^0 decay yields is shown in

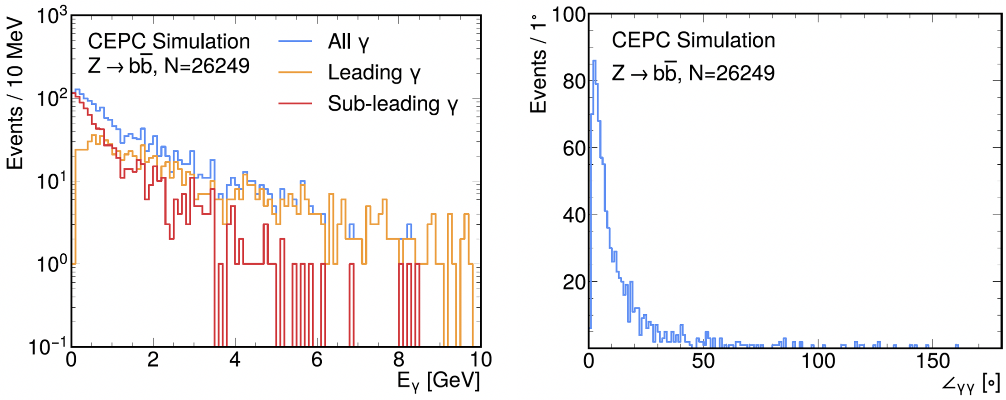

Figure 15.26

Table 15.14. These decays have fully hadronic final states. Data collected by the LHCb experiment during its Run-2 period (approximately 6 fb^{-1}) and the expected data to be collected over the entire lifetime of the LHC and LHCb (approximately 300 fb^{-1}), as well as the number of corresponding decay modes expected to be collected at the CEPC Z-pole operation mode are shown. Additionally, we compared the number of relevant decay modes reconstructed in certain physics analyses.

Despite the lower reconstruction efficiency, LHCb has a significant statistical advantage over CEPC for D^0 decays to fully charged hadronic final states. However, from the comparison listed in Table 15.14, it can be concluded that as a hadronic collider, LHCb experiment has particularly low efficiency for reconstructing π^0 particles, and for decay modes with π^0 final states, LHCb does not have a statistical advantage over CEPC in terms of reconstructed decay events. Therefore, conducting flavor physics research involving π^0 particles at the CEPC, such as searching for CP violation in the $D \to \pi\pi\pi^0$ decay, is promising in achieving measurement results comparable to LHCb's precision.

15.2.8 Top quark mass and width

The top quark, the most massive elementary particle in the Standard Model, has a strong coupling to the SM Higgs boson, providing an excellent probe for precision measurements and new physics beyond the SM. To date, the top quark mass has been measured in hadron collider experiments, such as those conducted at the Tevatron and the Large Hadron Collider (LHC), through direct reconstruction of the invariant mass of decay products. The top quark mass precision till now is down to less than a half of GeV [37–40] and it is mainly limited by the systematic uncertainties, such as jet energy scale, which are very challenging to be reduced.

Looking ahead, electron-positron colliders will enable not only direct reconstruction measurements but also an alternative approach using a threshold scan of the center-of-mass energy near the $t\bar{t}$ production threshold. At the energy threshold of $t\bar{t}$, the $t\bar{t}$ production

Table 15.14: The number of (D^0) and related fully hadronic final state decay modes produced at the LHCb experiment during its Run-2 period (approximately 6 fb^{-1}) and the expected data to be produced over the entire lifetime of the LHC and LHCb (approximately 300 fb^{-1}), as well as the number of corresponding decay modes expected to be produced at the CEPC Z-pole operation mode. The total yields at LHCb is estimated using the cross-section measured by Ref. [34], the reconstructed and selected events from LHCb are obtained from Ref. [35, 36], while the reconstruction and selection efficiency at CEPC is assumed to be 10%.

Decays	**LHCb (6 fb^{-1})**	**LHCb (300 fb^{-1})**	**CEPC (4 Tera Z)**
D^{*+}	4.7×10^{12}	2.4×10^{14}	4.6×10^{11}
D^0 from D^{*+}	3.2×10^{12}	1.6×10^{14}	3.1×10^{11}
$D^{*+} \to (D^0 \to K^-K^+)\pi^+$	1.6×10^{10}	6.5×10^{11}	1.3×10^{9}
$D^{*+} \to (D^0 \to \pi^-\pi^+)\pi^+$	4.6×10^{9}	2.3×10^{11}	4.5×10^{8}
$D^{*+} \to (D^0 \to K^-\pi^+)\pi^+$	1.6×10^{11}	6.3×10^{12}	1.2×10^{10}
$D^{*+} \to (D^0 \to \pi^-\pi^+\pi^0)\pi^+$	4.8×10^{10}	2.4×10^{12}	4.6×10^{9}
$D^{*+} \to (D^0 \to K^-\pi^+\pi^0)\pi^+$	4.6×10^{11}	2.3×10^{13}	4.4×10^{10}
Reco. & Sel. $D^0 \to K^-K^+$	5.8×10^{7}[35]	2.9×10^{9}	1.3×10^{8}
Reco. & Sel. $D^0 \to \pi^-\pi^+$	1.8×10^{7}[35]	9×10^{8}	4.5×10^{7}
Reco. & Sel. $D^0 \to K^-\pi^+$	5.2×10^{8}[35]	2.6×10^{10}	1.2×10^{9}
Reco. & Sel. $D^0 \to \pi^-\pi^+\pi^0$	2.5×10^{6}[36]	1.2×10^{8}	4.6×10^{8}
Reco. & Sel. $D^0 \to K^-\pi^+\pi^0$	1.9×10^{7}[36]	9.6×10^{8}	4.4×10^{9}

cross-section increases sharply as shown in Fig. 15.27 and is highly sensitive to the top quark mass, its decay width, and the strong coupling constant, α_S. The threshold scan method has been extensively discussed in the literature as a precise method for determining the top quark mass in the scenarios of ILC, CLIC, FCC-ee and CEPC [41–46].

In the CEPC setup, realistic scan strategies at the threshold are discussed to maximise the sensitivity to the measurements individually and simultaneously in the CEPC scenarios assuming a total luminosity limited to 100 fb^{-1} in Ref. [46]. With the optimal scan for individual property measurements, the top quark mass precision is expected to be 7 MeV considering only the statistical uncertainty. Taking into account the systematic uncertainties from theory, width, α_S, experimental efficiency, background subtraction, beam energy and luminosity spectrum, the top quark mass can be measured at a precision of 21 MeV optimistically and 54 MeV conservatively at CEPC, as shown in Tab. 15.15.

In Tab. 15.15, two scenarios of systematic uncertainties are considered, the optimistic and conservative ones. The experimental efficiency of future detectors is not yet known. To address this, we consider several possible scenarios for the level of uncertainty: 0.5%, 1%, 3%, and 5%. This uncertainty directly affects the signal yields, resulting in corresponding measurement uncertainties in the top quark mass of 4 MeV, 9 MeV, 26 MeV, and 44 MeV, respectively, which can be leading among all systematics uncertainties. The theoretical calculation uncertainty is assumed to be 3%, based on conservative estimates from Ref. [47,

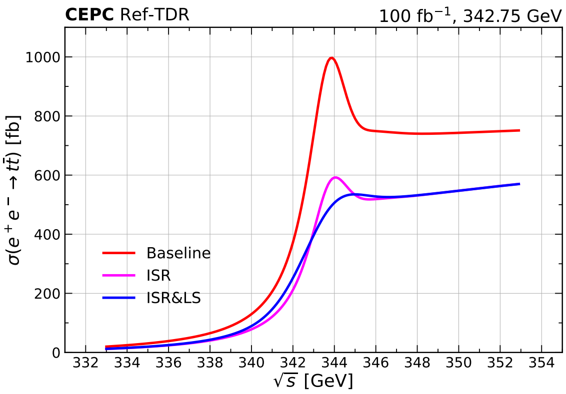

Figure 15.27: Cross section of $t\bar{t}$ production as a function of center-of-mass energy at CEPC [46], including the cross-section values without ISR or LR (baseline), the ones with ISR only and the ones with both ISR and LS.

Source	m_{top} precision (MeV)	
	Optimistic	Conservative
Statistics	7	7
Theory	8	24
Quick scan	2	2
α_S	16	16
Top width	5	5
Experimental efficiency	4	44
Background	1	3
Beam energy	2	2
Luminosity spectrum	3	6
Total	21	54

Table 15.15: The expected statistical and systematical uncertainties of the top quark mass measurement in optimistic and conservative scenarios at CEPC.

48], and 1%, anticipated to be achievable by the time of the experiments. This assumption aligns with that of Ref. [42]. A 1% and 3% uncertainty in the cross-section correspond to measurement uncertainties in the top quark mass of 8 MeV and 24 MeV, respectively, which are comparable to the level of the statistical uncertainty and three times larger than it. For details of other uncertainties considered in the list, please find them in Ref. [46].

All these estimations are based on the CEPC setup with the latest detector design, using a b-tagging efficiency of about 90% and a lepton identification efficiency of about 66%, which are the leading factors in determining the overall acceptance. The semi-leptonic and full hadronic channels of $t\bar{t}$ are studied. Their corresponding acceptance $\times$ efficiencies are 44% and 62%, respectively. In terms of the beam parameters, the beam energy could vary 2.6 MeV as estimated from the accelerator team. This impacts the measurement of top quark mass maximally by 2 MeV, below the statistical uncertainty, consistent with studies in LEP [49, 50] and of ILC [51] that showed small impacts on the top quark measurements in Ref. [42]. The variations on the spread of the luminosity spectrum can lead to uncertainties on the top quark mass measurement of 3 MeV and 6 MeV, if 10% and 20% are considered, respectively. These are quite different than the CLIC scenario in Ref. [42] given the different controls of the luminosity spectrum in circular and linear colliders.

15.2.9 W fusion cross section

The Higgs width is crucial for determining the absolute value of couplings to Higgs, making it essential for testing the electroweak symmetry breaking (EWSB) mechanism. A model-independent measurement of the Higgs decay width provides an inclusive test of EWSB and imposes constraints on beyond-Standard-Model (BSM) scenarios.

Currently, the only experimental measurements of Higgs properties come from the LHC. While the Standard Model (SM) predicts a Higgs width of only a few MeV, on-shell direct measurements at the LHC can only set an upper limit of a few GeV. Off-shell data, however, allows tighter constraints at the level of tens of MeV. Assuming the Higgs width equals the sum of partial widths for detectable decay channels, percentage-level precision can be achieved. However, this approach is unsuitable for EWSB tests or BSM physics due to its *a priori* assumptions.

Future lepton colliders, such as the proposed Circular Electron-Positron Collider (CEPC), will enable Higgs width measurements at the percentage level. The CEPC is expected to operate at two energy stages:

- $240\,\mathrm{GeV}$ with an integrated luminosity of $20\,\mathrm{ab}^{-1}$,
- $360\,\mathrm{GeV}$ with $1\,\mathrm{ab}^{-1}$.

At $360\,\mathrm{GeV}$, the ZH production cross-section is 36% lower than at $240\,\mathrm{GeV}$, while WW and ZZ fusion Higgs production cross-sections increase by factors of 3.8 and 4.6, respectively. These channels are critical for Higgs width determination. While the $240\,\mathrm{GeV}$ data alone provides excellent precision, the $360\,\mathrm{GeV}$ run offers an independent measurement. The combined precision of the Higgs width determination with the two runs can reach a remarkable precision.

The visible final states of signal are a pair of b jets. The main backgrounds is $ZH \to \nu\bar{\nu}b\bar{b}$. They have same final states and similar distribution in phase space. For the SM backgrounds. The 2 fermions backgrounds qq are the major backgrounds, due to its large cross-section. Then the irreducible backgrounds including ZZ, SZ are also the major backgrounds. The WW and SW which visible final states are a pair of jets plus one charged lepton are also needed to be considered. Backgrounds can be determined very well in theory and experiments, except the interference between the ZH and the WW which is difficult to be generated. It can be extracted by subtracting ZH and WW contributions from the inclusive $\nu\bar{\nu}H(H \to b\bar{b})$ sample.

Table 15.16 shows the cut flow for signals and backgrounds. Signal and ZH processes retain ¿50% efficiency after cuts, while 2-fermion backgrounds are suppressed to 0.2%. Other backgrounds become negligible.

Table 15.16: Cut flow for signal and background processes.

Process	WW	ZH	qq	SW	WW	SZ	ZZ
Pre-selection	17209	4930	2123258	117427	1686000	178340	266300
$30 < \mathrm{NPFO} < 180$	17196	4927	2103067	117105	1674708	172670	262188
$100\,\mathrm{GeV} < E < 250\,\mathrm{GeV}$	16667	4860	1501935	44023	468516	171306	151500
$p_T > 10\,\mathrm{GeV}$	16272	4847	249395	43119	456289	148885	145116
Lep-veto	15751	4611	245141	16366	187787	147061	141445
$100\,\mathrm{GeV} < m_{\text{total}} < 150\,\mathrm{GeV}$	14291	4055	62897	6744	47649	21893	24613
$50\,\mathrm{GeV} < m_{\text{recoil}} < 250\,\mathrm{GeV}$	14092	3765	40763	3674	26876	16802	14198
$y_{12} > 0.10$	12982	3030	33885	1707	12636	13114	9297
$-0.99 < \cos_{ij} < 0.25$	12742	2789	25714	1368	8154	10489	5658
b-tag	11499	2517	4650	13	78	1897	1023

The signal strength is determined by fitting the recoil mass, recoil angle, or both. Figure 15.28 shows fitting results with precisions of 2.9% (recoil mass) and 4.5% (recoil angle).

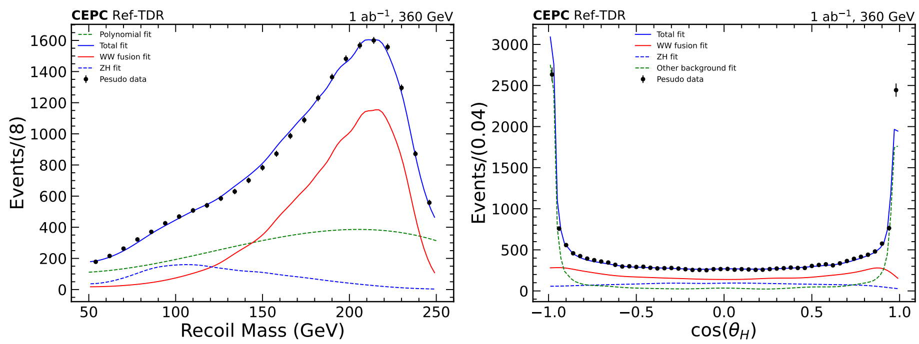

Figure 15.28: Fitting to the Asimov data on recoil mass (left) and recoil angle (right)

15.2.10 Long-lived particles

The hypothesis that BSM particles could possess long lifetimes, evading detection, has transitioned from a nascent idea to a widely accepted and vigorously pursued avenue within the physics community. These particles, often called long-lived particles (LLPs), serve as sensitive probes into BSM physics. The Higgs boson production via $e^+e^- \to ZH$ at these colliders offers a clean channel to explore rare LLP decays, benefiting from well-defined initial states and reduced backgrounds compared to hadron colliders.

The Higgs particle can decay into LLPs (X) via two decay modes with two jets or leptons. In the lepton scenario, such as the $H \to XX \to$ lepton. The decay of LLPs can yield either a 2-lepton or a 4-lepton final state, depending on the specific LLP decay model. In this study, we focus on the 2-lepton channel, which includes both dielectron (2e) and dimuon (2μ) final states. The distinctive signature is a displaced vertex accompanied by two leptons. We generated 15 signal samples covering the regions of the LLP parameter space, with masses of 1, 10, and 50 GeV and lifetimes ranging from 0.001 ns to 100 ns. The dominant background processes include ZH production, 2-fermion processes with electrons or muons, and 4-fermion processes such as $ee \to ZZ \to ll\nu\nu$.

This analysis utilizes the tracking and lepton ID performance of the CEPC detector. The events are selected by the lepton pairs after particle ID with momentum larger than 3 GeV. After the selection of $N_{\text{PFOs}} < 20$ to remove the jets, following selections are applied to suppress background:

- $\Delta\theta$ cut: the difference in theta plane.
- Z veto: mass window cut with $|M_{ll} - 90| < 10$ GeV.
- M_{recoil}: the recoil mass of the lepton pairs.
- $\Delta T_j = \Sigma(t_{\text{hit},i} - r_{\text{hit},i}/c)$: the minimal time difference, where $t_{\text{hit},i}$ represents the hitting time of the i^{th} hit in the TOF detector and $r_{\text{hit},i}$ is the i^{th} Euclidean distance to IP, and c the light speed in vacuum.

The detailed cuts are optimized according to the mass of LLPs, the 2 channels are further selected in below:

- The 2μ channel: events should only have a muon pair in opposite charge passing the best muon ID WP. After the Z-veto and recoiled mass cut $M_{recoil} < 140$ GeV. The $\Delta\theta_{\mu\mu} < 50$ (20) degree and the $\Delta T_j > 0.15$ (0.1) for $m_\chi = 10, 50$ (1) GeV.
- The 2e channel: same as the selection criteria of the 2μ channel except the lepton ID,and ΔT. The $\Delta T_j > 0.05$ (0.01) for $m_\chi = 10, 50$ (1) GeV.

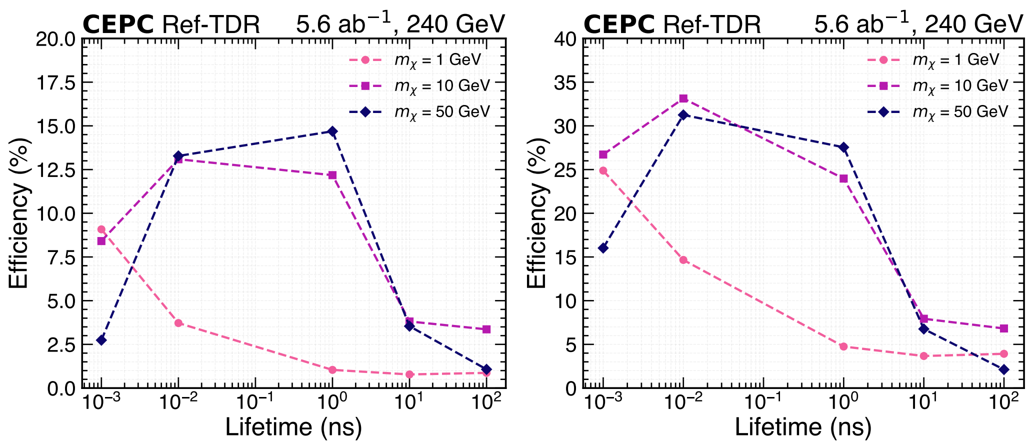

Figure 15.29: The signal efficiency of the LLPs with different lifetime in 2μ channel(left plot) and 2e channel (right plot).

The Figure 15.29 shows the result of the signal efficiency after event selection. The signal efficiency reaches 12% in 2μ channel and 30% in 2e channel when $m_\chi = 10$ GeV.

The backgrounds efficiency are shown in the table. For the jet scenario, such as $H \to XX \to$ jets process, the study using machine learning method is presented in [52], with the signal efficiency up to 99% with nearly background free assumption.

15.2.11 Supersymmetric muon

The Supersymmetrized Standard Models (SSMs) bring many appealing features, including gauge coupling unification, and dynamical electroweak symmetry breaking, and provide a comprehensive theory framework for novel phenomena. For example, the Lightest Supersymmetric Particle (LSP) can serve as a viable dark matter (DM) candidate with R-parity conservation.

As designed for lower energy, CEPC can cover important parameter spaces at low mass region, especially at very compressed mass region that is difficult for a high-energy pp collider to reach. Light smuon particle is interesting to search for at the CEPC, which favored by SUSY explanations to dark matter relic density requirements. This analysis [53] will focus on the charged smuon pair production with subsequent decay into a final state with two-muon and missing energy from two $\tilde{\chi}_1^0$, which is LSP. This analysis can also check the muon and missing energy performance from corresponding sub-detectors, such as muon detector and calorimeter etc.

Events containing exactly two opposite sign (OS) muons with energies above 1.0 GeV are selected. The recoil system consists of all the particles except the two OS charged leptons, which including invisible particles such as neutrinos and neutralinos. The following variables are efficient in discriminating the signal events from SM backgrounds:

- $\Delta R(\mu, \text{recoil})$[1], the angular distance between one muon and the recoil system.
- E_μ, the energy of one muon.
- $M_{\mu\mu}$, the invariant mass of two muons.
- M_{recoil}, the invariant mass of the recoil system.

The signal regions are defined using the above kinematics selection criteria. To estimate the sensitivity of the signals, the median significance is used, which can provide a much better approximation to the true significance in regions where the number of signal events is not negligible, denoted here by Zn [54]. The statistical uncertainty and 5% flat systematic uncertainty are considered in the Zn calculation.

Three signal regions (SRs) are developed to cover different mass splitting between $\tilde{\mu}$ and $\tilde{\chi}_1^0$ (ΔM). The SR-ΔM^h covers the region with high ΔM, the SR-ΔM^m covers the region with medium ΔM, and the SR-ΔM^l covers the region with low ΔM. To improve the signal sensitivity, SR-ΔM^h and SR-ΔM^m signal regions are divided in $E_{\mu 1,2}$ intervals. The signal regions definition is summarized in Table 15.17. The E_μ selections are required

[1] $\Delta R = \sqrt{(\Delta\eta)^2 + (\Delta\phi)^2}$, where η is the pseudorapidity which defined in terms of the polar angle θ by $\eta = -\ln\tan(\theta/2)$ and ϕ is the azimuthal angle.

to reject $\tau\tau$ and $Z\nu$ processes. The cuts on $\Delta R(\mu, \text{recoil})$ are used to suppress $\tau\tau$, $\mu\mu$ and ZZ processes, and the cuts on the $M_{\mu\mu}$ are used to suppress WW and $\mu\mu$ processes and other backgrounds including Z. According to the signal topology, most of the signal events have large recoil mass. So, a lower cut of the invariant mass of recoil system, M_{recoil}, has been used to reject $\mu\mu$ and Z or W mixing processes and some other SM processes without large recoil mass. The main background contributions in the SRs are from ZZ or $WW \to \mu\mu\nu\nu$, $\mu\mu$, $WW \to \ell\ell\nu\nu$, $ZZ \to \mu\mu\nu\nu$, $\tau\tau$, ZZ or $WW \to \tau\tau\nu\nu$ and $\nu Z, Z \to \tau\tau$ processes.

<table>
<tr><th>SR-ΔM^h</th><th>SR-ΔM^m</th><th>SR-ΔM^l</th></tr>
<tr><td>$E_{\mu 1,2} > 40$ GeV</td><td>$9 < E_{\mu 1,2} < 48$ GeV</td><td rowspan="2">–</td></tr>
<tr><td>$E_{\mu 1,2} \in (40-50, > 50)$ GeV</td><td>$E_{\mu 1,2} \in (9-25, 25-48)$ GeV</td></tr>
<tr><td>$\Delta R(\mu, \text{recoil}) < 2.9$</td><td colspan="2">$1.5 < \Delta R(\mu, \text{recoil}) < 2.8$</td></tr>
<tr><td>$M_{\mu\mu} < 60$ GeV</td><td>$M_{\mu\mu} < 80$ GeV</td><td>–</td></tr>
<tr><td>$M_{\text{recoil}} > 40$ GeV</td><td>–</td><td>$M_{\text{recoil}} > 220$ GeV</td></tr>
</table>

Table 15.17: Summary of selection requirements for the direct smuon production signal region. ΔM means difference of mass between $\tilde{\mu}$ and $\tilde{\chi}_1^0$.

The expected sensitivities as function of $\tilde{\mu}$ mass and $\tilde{\chi}_1^0$ mass for the signal regions with systematic uncertainty of 0 – 5% for direct smuon production are shown in Figure 15.30. For each signal point, the signal region with best Zn has been chosen. With the assumption of 5% flat systematic uncertainty, the discovery sensitivity can reach up to 119 GeV depending on different LSP mass with smuon mass, which is not too much effected by systematic uncertainty of detectors.

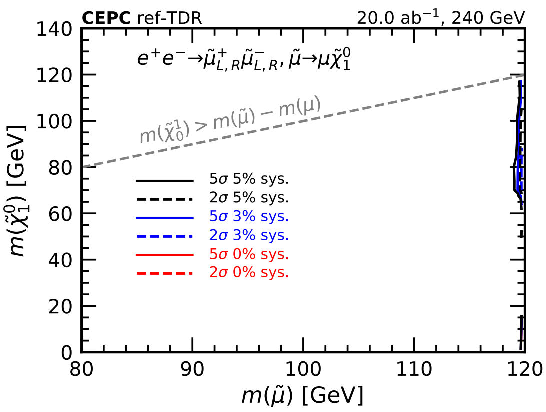

Figure 15.30: The prospected exclusion contours and discovery contours at CEPC for the direct $\tilde{\mu}$ production with 0 - 5% flat systematic uncertainty.

15.2.12 A_{FB}^{μ} ($e^+e^- \to \mu^+\mu^-$) at Z pole

The CEPC data at Z pole energy allow high precision electroweak measurements of the Z boson properties, such as the forward-backward charge asymmetry (A_{FB}) as a function of the effective weak mixing angle. The $\mu^+\mu^-$ channel is one of the cleanest final state at Z pole. The physics analysis benchmark in this channel offers the simplest verification of the detector acceptance, reconstruction of particle-flow objects (PFO), and identification of muons. Hence, the measurement of A_{FB} with the $e^+e^- \to \mu^+\mu^-$ process is a good example of the physics analyses. The forward-backward asymmetry is defined in terms of the angle θ_{CM} between the negatively charged final-state muon and the initial-state electron in the di-lepton center-of-mass frame.

$$A_{FB} = \frac{\sigma_F - \sigma_B}{\sigma_F + \sigma_B} \tag{15.6}$$

where σ_F (σ_B) is the total cross section for forward (backward) events, defined by $\cos\theta_{CM} > 0 (< 0)$. θ_{CM} is the θ_{μ^-} recomputed at the center-of-mass frame of the di-lepton system. The sign of θ_{CM} is defined so that $\cos\theta_{CM} = 1$ events are those in which the negatively charged final-state lepton is traveling in the same direction as the incident electron.

When the collision energy is close to the Z boson mass peak, A_{FB} reflects pure Z exchange and is close to zero because of the small value of the charged-lepton vector coupling to Z bosons. The combination of LEP measurement yields a value of $A_{FB}^{\mu} = 0.0163 \pm 0.0014$ in the $\mu^+\mu^-$ channel. At CEPC, the statistical uncertainty of A_{FB}^{μ} can be significantly reduced, the major contributions to the total uncertainty are expected to come from systematic sources, such as the energy spread uncertainty, and the energy and angular resolution of the reconstructed PFO.

The signal and background events are simulated with Whizard+Phythia at LO. The W and Z boson mass (width) values are set precisely to their latest measured values of 80.377 (2.085) and 91.1876 (2.4952) GeV. The interference between Z and γ^* has been included, and the initial-state-radiation (ISR) and final-state-radiation (FSR) are on in the simulation. The predicted A_{FB}^{μ} is 0.0161 ± 0.0010 by simulating 1 million events, which is consistent with the LEP result.

The $e^+e^- \to \mu^+\mu^-$ events are selected by identifying opposite-charge muon pairs. The muons are required to pass $p_{\mathrm{T}} > 1$ GeV, $\cos\theta < 0.99$, and the muon identification requirements (the "Best" working point). A ± 10 GeV Z mass window is required to reject the background with genuine muons, which are mainly $e^+e^- \to \tau^+\tau^-$ and $e^+e^- \to b\bar{b}$ events. Finally a $|\cos(\theta_{\mu^-})| > 0.05$ cut is applied to remove the migrations between forward and backward regions.

Figure 15.31 presents the p_{T} and $\cos(\theta_{CM})$ distributions of the geninue and reconstructed μ^-, the ratio pads show the total event selection efficiency.

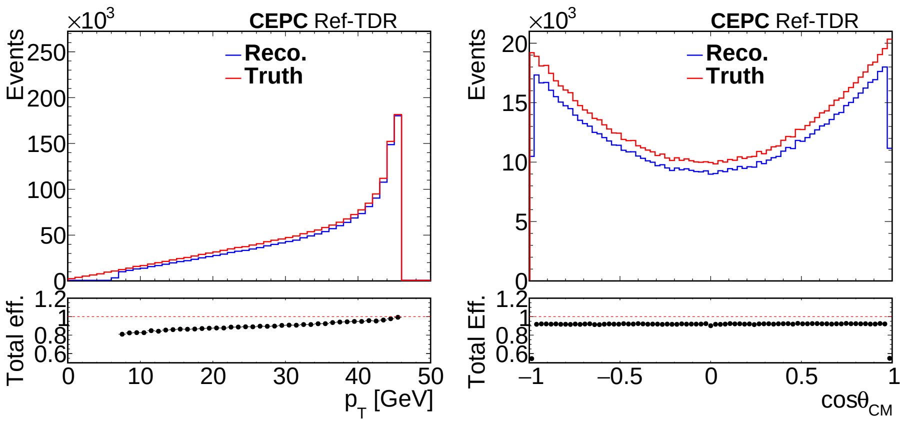

Figure 15.31: (Left) The distribution of μ^- p_{T} at the lab frame. (Right) The distribution of μ^- $\cos(\theta_{CM})$ at the center-of-mass frame. The ratio pads show the total event selection efficiency.

Table 15.18 shows the selection efficiencies of signal and background. The signal efficiency is around 90%, while the background efficiencies are lower than 0.005%, the main background is $e^+e^- \to \tau^+\tau^-$, and other backgrounds are negligible.

Table 15.18: The cross-section, number of simulated events, and selection efficiencies of signal, $e^+e^- \to \mu^+\mu^-$, and background, $e^+e^- \to \tau^+\tau^-$ and $e^+e^- \to b\bar{b}$.

	$e^+e^- \to \mu^+\mu^-$	$e^+e^- \to \tau^+\tau^-$	$e^+e^- \to b\bar{b}$	$e^+e^- \to e^+e^-$
Cross-section	1.2 nb	1.2 nb	6.6 nb	1.2 nb
Simulated events	982476	185855	44550	32397
A pair of muons	967262	5135	1035	0
Z mass window	903640	5	0	0
Muon $\lvert\cos(\theta)\rvert > 0.05$	869450 (88.5%)	5 (0.003%)	0 (<0.002%)	0 (<0.003%)

Since the fraction of signal events is close to 100% after the event selection, the A^{μ}_{FB} is directly calculated by counting the forward (backward) events, by judging $\cos(\theta_{CM}) > 0 (< 0)$. The A_{FB} calculated in the signal region, A^{obs}_{FB}, is in a particular phase space, it is usually larger than the A_{FB} in SM because of the Z mass window cut. The A^{obs}_{FB} will be corrected back to the full phase space with the MC samples to get the final result of A_{FB}. Table 15.19 shows the number of forward (backward) events and the corresponding A^{μ}_{FB}, from simulation and after reconstruction. The measured value of A^{μ}_{FB} has 9×10^{-6} difference compared to the simulated value, which is taken as one systematic variation.

The statistical uncertainty of A^{μ}_{FB} is extrapolated from 10^6 muon pairs in the simulated sample, to two assumptions:

- Nominal result: extrapolating to 1.35×10^9 muon pairs expected during the one-month low-luminosity Z running in the first year of ZH operation, the statistical uncertainty of A^{μ}_{FB} in this case is 3.1×10^{-5}.

- Alternative: extrapolating to 1.38×10^{11} muon pairs expected during 2 years of Z pole data taking, the statistical uncertainty is 3×10^{-6}.

Table 15.19: The number of forward (backward) events and the corresponding A^{μ}_{FB}, from simulation, after selection, and after reconstruction.

	MC particles wo selections	**after selections**	**Using PFO**
Forward ($\cos(\theta_{CM}) > 0$)	499136	442727	442723
Backward ($\cos(\theta_{CM}) < 0$)	483340	426723	426727
A^{μ}_{FB} or A^{obs}_{FB}	0.016078	0.018407	0.018398
Corrected A^{μ}_{FB}			0.016070

Several systematic uncertainty sources are considered and their estimation is described below:

- Uncertainty from object mis-identification of the muon: the probability and impact of selecting wrong pairs of PFO from the signal events was found negligible.
- Uncertainty from background: by comparing the A^{obs}_{FB} with / wo background events, the uncertainty is measured to be 1×10^{-6}.
- Uncertainty from the detector acceptance and resolution of $|\cos(\theta_{\mu^-})|$ and $p^{\mu^-}_{\mathrm{T}}$: apply event selections on the MC particles instead of PFO, and compare the results. This uncertainty is estimated to be 9×10^{-6}.
- Uncertainty from energy spread: A^{μ}_{FB} varies as a function of center-of-mass energy, and according to CEPC accelerator TDR, the beam energy spread at Z pole is 0.13%. A set of $e^+e^- \to \mu^+\mu^-$ samples were simulated at different energy values, and a parameterization of $A^{\mu}_{FB}(E_{CM})$ is done. The uncertainty of beam energy spread is estimated by comparing the A^{μ}_{FB} with / wo energy spread, assuming beam energy follows a Gaussian distribution. The uncertainty is measured to be 2×10^{-5}.

An alternative method fitting the $\cos(\theta^{\mu^-}_{CM})$ distribution was also investigated, the fitting method is treated as a verification of the counting method, and it brings consistent results within the statistical fluctuations of the simulated sample.

Conclusion: this analysis measures the forward-backward asymmetry with $e^+e^- \to \mu^+\mu^-$ events at Z pole (A^{μ}_{FB}). The uncertainty of measurement is ±0.000031 (stat.) ± 0.000022 (syst.) based on the dataset from the first year of ZH operation. The CEPC result improves the precision of LEP result (±0.0014) by two magnitudes.

15.3 Challenges and Plan

15.3.1 Strategy for measuring absolute luminosity

Precision measurement of the integrated luminosity $\mathcal{L}_{\text{int}}$ is crucial for the realization of the physics program at CEPC. This is particularly true for the $Z-$pole cross-section measurement, determination of the $Z-$width from the line-shape of $e^+e^- \to 2f$ production and the measurements of the W boson mass and width from the line-shape of the cross-section of $W-$pair production near the threshold. At the $Z-$pole, the relative uncertainty of $\mathcal{L}_{\text{int}}$ is required to be of the order of 10^{-4}, while 10^{-3} should suffice at higher center-of-mass energies.

The strategy for achieving the required precision of absolute luminosity measurement involves an iterative process, including the identification of SM processes, monitoring and calibration of detector response, and high-precision calculation.

A compact EM calorimeter has been designed to function as luminometer, as discussed in Section 3.4. Experimental precision of the integrated luminosity is dependent on several sources of uncertainty, including the luminometer's resolution in terms of position and energy measurement of Bhabha showers. The position resolution of Bhabha hits in the luminometer front plane can be improved to a micron level by placing a Si-tracking plane in front of the luminometer, which provides enhanced electron-photon separation.

Uncertainties in $\mathcal{L}_{\text{int}}$ measurement may arise from various misalignments of the detector arms with respect to each other and the interaction point (IP), as well as from the uncertainties related to finite beam sizes and beam delivery to the IP. These uncertainties collectively referred to as metrological uncertainties, are discussed in Section 3.4. Detailed studies[55] have shown that achieving the targeted precision is feasible at CEPC, both at 240 GeV and during the $Z-$pole operation. The major challenge at the $Z-$pole arises from the need to control the inner aperture of the luminometer at the micron level. A dedicated laser-based system for luminometer position monitoring must be developed, with technologically feasible precision margins set in [55]. Systematic uncertainties in integrated luminosity measurement originating from beam-beam interactions have also been studied [56], showing a comparable impact as at the FCCee [57], and being less pronounced than at linear e^+e^- colliders due to less compact bunches. The impact of the beam energy spread on $\mathcal{L}_{\text{int}}$ measurement is discussed in [58], as well as the precision required to determine it from the luminosity spectrum obtained from di-muon production at CEPC. The possibility of using other SM EW processes, such as $ee \to \gamma\gamma$, to determine the luminosity is also under assesment.

For the $e^+e^- \to e^+e^-$ process, theoretical uncertainty is limited by the hadronic vacuum polarization at the level of 10^{-4}, while for the $e^+e^- \to \gamma\gamma$ process, the contribution of hadronic loops is less than 10^{-5} [59]. The current uncertainty of MC generators for the $e^+e^- \to \gamma\gamma$ process is 10^{-3} at M_Z, for instance, with the BABAYaga NLO [60]. When NNLO corrections from [59] are applied, reaching an accuracy of $\sim 10^{-4}$ could be possible. To achieve an accuracy of 10^{-4} to 10^{-5}, a comprehensive calculation of NNLO QED corrections and, eventually, two-loop weak contributions will be required.

The process of two-photon annihilation of e^+e^- at energies above the Z boson mass has been studied at the LEP collider [61]. Each of the four detectors observed approximately 5000 events, indicating that the process was primarily observed with statistical uncertainty being dominant. The most accurate result was obtained with the OPAL detector [62], where systematic uncertainty reached 0.56%. The major part of this systematic uncertainty (0.46%) was related to the photon conversion probability, limited by the available statistics of photon events. At CEPC, the conversion probability can be expected to be well studied due to the large statistics of photon events.

At CEPC, the process $e^+e^- \to \gamma\gamma$ can be utillized for determining luminosity offline, provided there is a sufficiently large data set (at least 3.3 ab^{-1} is needed to achieve 10^{-4} accuracy). The advantage of using this process lies in the capability of the main detector to determine luminosity, which helps reduce systematic uncertainties in relative luminosity measurement. The reduction in systematic uncertainties can be confirmed by comparing the ratio of the number of $\gamma\gamma$ events to e^+e^- events under consistent selection conditions with theoretical predictions.

15.3.2 Application of the resonant depolarization method for the W/Z boson mass determination

The resonant depolarization technique, which employs a pulsed "depolarizer" with frequency-scan capability to induce a narrow artificial spin resonance for beam depolarization, and measures the location of depolarization with the precisely known depolarizer frequency, currently provides the most precise measurements of the beam energy. Its implementation at the CEPC would require achieving transverse polarization levels of at least 5% to 10% for both beams. This also necessitates the implementation of laser-Compton polarimeters capable of measuring the vertical beam polarization with a resolution of 1% every few seconds. Additionally, tracking the evolution of beam energies throughout the physics runs is essential for the precision measurements of W/Z masses. This requires conducting resonant depolarization measurements frequently, approximately every 10–15 minutes, where each measurement will depolarize one or two bunches for each particle species and determine the instant beam energy. Interpolation can then be used to model the evolution of the beam energies more precisely.

As detailed in the CEPC Accelerator TDR [63] and references therein, besides the scheme of using self-polarization in the collider rings [64] which can generate above 10% polarization in about 2 hours, particularly with the help of asymmetric wigglers at the Z-pole, it is also viable to prepare polarized lepton beams from the source. These beams can be transported throughout the injector chain and injected into the collider rings to meet the requirements of beam energy calibration. The strategy involves utilizing one or two bunches per species that can be efficiently depolarized. Once depolarized, they can be readily removed and replaced with new polarized bunches. This process aligns with the capabilities of the injector chain, ensuring a streamlined calibration procedure, and can deliver above 50% polarized electron bunches and above 20% polarized positron bunches. Availability studies [65], including failures of systems like RF systems or power converters, suggest that the latter approach could promise much less physics dead time and a substantial increase in the integrated luminosity.

Note that this approach requires some modification of the entire injector chain as outlined in the CEPC Accelerator TDR and should be implemented in an updated design. Additionally, preparing electron beams with over 85% polarization from the source is achievable with status-of-the-art technology, and this approach has the potential to realize over 50% longitudinal polarization for colliding beam experiments. There is a 400 kV photocathode DC gun at the Platform of Advanced Photon Source Technology R&D (PAPS) managed by IHEP, and there are ongoing efforts to convert it to a polarized electron source and build associated beamline to measure the beam polarization, in addition to domestic fabrication of the superlattice GaAs/GaAsP photocathodes. The plan is to have first experiments of polarized electron beam generation in 2027.

To prepare for the high performance of Compton polarimetry, polarized electron sources and resonant depolarization techniques to be used in CEPC, dedicated R&D efforts have been underway in the EDR phase of the CEPC. In particular, a Compton polarimeter is being constructed at BEPCII, reusing the hutch and beamline of a dismantled wiggler, to measure the vertical polarization of the electron beam in the storage ring due to the self-polarization build-up. Although this Compton polarimeter is based on detecting backscattered γ photons, rather than the preferred solution of detecting backscattered electrons as planned for CEPC, it will establish the know-how to operate such a delicate instrument, as well as advance laser polarization control and pixel detector technologies for Compton polarimetry. The conceptual design of the Compton polarimeter has been finalized, and modification of the beamline and the hutch region has been completed. The first beam experiment of the Compton polarimeter is underway.

Once reliable beam polarization measurements are achieved, demonstration of beam energy calibration with the resonant depolarization technique is foreseen at BEPCII in the coming 2-3 years. Being a double-ring collider with many bunches similar to CEPC, BEPCII will serve as an ideal test bed for the operational concepts of resonant depolarization for CEPC, for example using dedicated pilot bunches for resonant depolarization and continuous monitoring of the beam energy throughout physics runs.

The knowledge gained through these R&D activities will set a solid foundation for the practical design of Compton polarimetry and preparation for resonant depolarization applications at CEPC.

15.3.3 Methods and considerations for Calibration, Alignment

This section summarizes the calibration and alignment strategies for CEPC subdetectors, combining physics-driven methods and technical monitoring to meet the required performance for precision measurements.

Vertex Detector Calibration and Alignment Vertex alignment is based on $Z \to \mu^+\mu^-$ events, minimizing track-hit residuals through iterative geometry updates. Sub-10 μm accuracy is achieved, with impact parameter resolution validated using displaced $K^0_S \to \pi^+\pi^-$ vertices. Thermal and mechanical shifts are monitored over time, with correction maps derived from residual drifts. Temperature variations of 1°C can induce micron-level misalignments. Temporal stability is cross-checked using photon conversions and K^0_S events.

Charge collection efficiency is monitored with e^+e^- pairs from conversions, and pixel gain equalization uses MIP tracks to reduce response variation. Inter-layer timing alignment is calibrated using relativistic muons, reaching synchronization better than 0.5 ns. Radiation effects are tracked via MIP signal trends, with all sensors pre-tested for long-term stability.

Tracker Calibration and Alignment The CEPC tracking system, comprising silicon trackers and a TPC, is calibrated for geometry, momentum scale, and timing. Initial alignment uses cosmic and beam halo muons to reduce residuals below 10 μm (silicon) and 100 μm (TPC).

Momentum calibration employs Z, J/ψ, and Υ resonances. Deviations in invariant mass are used to extract per-module corrections, combined via momentum-weighted averages.

OTK and TPC timing is calibrated using tau decay chains and cosmic muons. In the TPC, UV laser tracks calibrate drift velocity and correct space charge effects. Timing resolution reaches 50 ps for OTK and 100 μm spatial precision for the TPC.

A Kalman filter refines alignment using $Z \to \mu^+\mu^-$ events, reducing residuals to design-level precision. Real-time monitoring involves tracking channel efficiency and making environmental corrections based on both temperature and radiation dose, ensuring optimal performance.

Laser interferometry tracks mechanical shifts at micron scale. Structural expansion is modeled and combined with track-based alignment to maintain long-term stability.

ECAL Calibration and Alignment ECAL calibration is performed using physics-driven and monitoring-based methods to ensure an electromagnetic energy resolution around $3\%/\sqrt{E}$.

The E/p technique, utilizing electrons from e^+e^- and W/Z decays, compares ECAL energy to tracker momentum to monitor gain drifts. Corrections are updated regularly based on time-dependent E/p trends.

Intercalibration employs $\pi^0 \to \gamma\gamma$ decays, reconstructing invariant masses and weighting energy contributions by crystal to derive per-channel constants. Iterative averaging and η-ring smoothing reduce local statistical fluctuations. The absolute scale is determined from $Z \to e^+e^-$ events by comparing reconstructed masses to the nominal Z mass. $J/\psi \to e^+e^-$ decays provide low-energy cross-checks.

Cosmic muons supply continuous monitoring of SiPM gain and transparency changes. Timing synchronization between channels is refined using relativistic muons, reaching alignment within 0.5 ns.

Track-based ECAL alignment extrapolates high-p_{T} tracker tracks to the calorimeter surface, minimizing residuals to refine module positions. Mechanical stability is monitored with strain sensors and laser lines, ensuring long-term alignment consistency.

HCAL Calibration and Alignment The HCAL is calibrated to achieve 3–4% jet energy resolution at 100 GeV, beginning with radioactive source scans and test beam calibration of modules during construction. These define initial channel gains and validate response uniformity across η and ϕ.

During operation, gain stability is maintained via LED/laser monitoring. Energy reconstruction applies corrections for light yield variation, intercalibration factors, and η-dependent scaling. Pileup suppression is performed with pulse-shape fits.

ϕ-symmetry is exploited to equalize response across η rings, using statistical moment methods. The absolute scale is tuned using isolated charged hadrons, comparing HCAL energy to tracker momentum after ECAL subtraction. Dijet and multijet events provide additional cross-checks via transverse balance and reconstructed W/Z masses.

SiPM gain and radiation damage are tracked with MIP response and temperature modeling. Alignment is derived from cosmic-ray muons traversing multiple layers, with geometry updated to minimize hit residuals. Structural sensors ensure sub-mm mechanical stability.

Muon Detector Calibration and Alignment For the muon system, channel efficiency and energy response are calibrated with $Z \to \mu^+\mu^-$ tracks, extrapolated from the tracker. MIP peaks and detection efficiency are extracted layer-by-layer. Cosmic muons complement this with absolute intercalibration, and responses are smoothed over η regions.

Muon ID performance is maintained using likelihood templates based on hit multiplicity and penetration depth, trained on muon and pion control samples. SiPM gain is monitored via cosmic MIPs and LED pulses, with corrections applied for temperature-induced variation and optical degradation.

Timing calibration uses dual-ended strip readout and waveform fitting, achieving sub-ns resolution after correcting propagation delays. Geometry alignment is refined by minimizing residuals between extrapolated tracks and measured hits using Z events and cosmics. Embedded mechanical sensors help monitor structural deformation, ensuring alignment stability over time.

15.3.4 Further technology decisions and detector optimization

Given the timing constraint of the current TDR study, there are several areas for further optimizations beyond this reference detector TDR results. These areas will be considered in the long term:

- ECAL Transverse Granularity for Boosted π^0/γ Separation
  We will evaluate the transverse granularity of the ECAL's long crystal bars to improve discrimination between boosted π^0 decays and single photons. This study will quantify the impact of finer segmentation on reconstruction algorithms and photon purity, particularly in high-occupancy regions.
- HCAL Thickness vs. Polar Angle for Jet Energy Resolution
  A parameterized analysis of HCAL thickness as a function of polar angle will be conducted to balance jet energy resolution against cost constraints. This includes optimizing the radial and longitudinal segmentation to mitigate energy leakage while minimizing cost.
- Muon System Optimization for Long-Lived Particle Searches
  The muon identification performance will be studied as a function of the number of muon detector layers. We will assess trade-offs between layer count, spatial coverage, and sensitivity to long-lived particles (e.g. displaced vertices), ensuring compatibility with background rejection requirements.
- Low-Momentum Charged Hadron PID with AC-LGAD Timing Layers
  To enhance the identification of low-momentum charged hadrons, which could not reach the Outer Tracker layer, a proposal is made to replace the outermost layer of the Inner Tracker with an AC-LGAD-based timing layer. This technology's combined spatial ($\sim 10\ \mu\mathrm{m}$) and timing (~ 50 ps) resolution could significantly improve $\pi/K/p$ separation without compromising tracking performance.

In terms of technology choices, several key performance-driven evaluations needed for detector subsystems include:

- Pixel vs. Strip ITK for PID Requirements
  A comparative study will assess the impact of using strip-based ITK instead of pixel sensors on particle identification (PID) capabilities. This includes evaluating resolution trade-offs, occupancy limits, and compatibility with the timing layer integration proposed above.

- Beam Background and TPC vs. Drift Chamber (DC) at High Luminosity Z pole run
  Beam-induced backgrounds will be simulated to quantify their impact on tracking subsystem choices (TPC vs. DC) during high-luminosity Z-pole running. Critical metrics include occupancy, hit reconstruction efficiency, and robustness against pileup.
- HTS Ultra-Thin Magnet Feasibility
  The potential use of High-Temperature Superconducting (HTS) magnets will be explored to reduce the solenoid's radial thickness while maintaining field strength. This study will address mechanical stability, quench protection, and integration with the detector's overall material budget.

15.4 Summary

With the reference detector design and full simulation, detailed performance of the fundamental objects have been evaluated, and a set of benchmarks have been conducted. They illustrate the detector performance for center-of-mass energies in the range from 91 GeV up to 360 GeV. All results obtained have been summarized in the following Tables - to be made. In addition, areas of challenges and plans beyond the current TDR are also identified.

References

[1] S. Agostinelli et al. "Geant4 - a simulation toolkit". In: *Nuclear Instruments and Methods in Physics Research A* 506 (2003), pp. 250–303.

[2] Tianqi Chen and Carlos Guestrin. "XGBoost: A scalable tree boosting system". In: *Proceedings of the 22nd ACM SIGKDD International Conference on Knowledge Discovery and Data Mining*. ACM. 2016, pp. 785–794.

[3] Taikan Suehara and Tomohiko Tanabe. "LCFIPlus: A framework for jet analysis in linear collider studies". In: *Nuclear Instruments and Methods in Physics Research Section A: Accelerators, Spectrometers, Detectors and Associated Equipment* 808 (2016), pp. 109–116. ISSN: 0168-9002.

[4] S. Catani et al. "New clustering algorithm for multijet cross sections in e+e- annihilation". In: *Physics Letters B* 269.3-4 (1991), pp. 432–438. ISSN: 0370-2693.

[5] M. Cacciari, G. P. Salam, and G. Soyez. "FastJet user manual". In: *The European Physical Journal C* 72 (2012), p. 1896.

[6] Torbjörn Sjöstrand, Stephen Mrenna, and Peter Skands. "A brief introduction to PYTHIA 8.1". In: *Computer Physics Communications* 178.11 (2008), pp. 852–867. ISSN: 0010-4655.

[7] Hao Liang et al. "Jet-Origin Identification and Its Application at an Electron-Positron Higgs Factory". In: *Phys. Rev. Lett.* 132 (22 2024), p. 221802.

[8] W. Kilian, T. Ohl, and J. Reuter. "WHIZARD - simulating multi-particle processes at LHC and ILC". In: *Eur. Phys. J. C* 71 (2011), p. 1742.

[9] Torbjorn Sjostrand, Stephen Mrenna, and Peter Z. Skands. "PYTHIA 6.4 Physics and Manual". In: *JHEP* 05 (2006), p. 026.

[10] CM Carloni Calame et al. "The BABAYAGA event generator". In: *Nuclear Physics B-Proceedings Supplements* 131 (2004), pp. 48–55.

[11] M. Beneke et al. "Near-threshold production of heavy quarks with `QQbar_threshold`". In: *Comput. Phys. Commun.* 209 (2016), pp. 96–115.

[12] The CMS Collaboration. "Observation of a new boson at a mass of 125 GeV with the CMS experiment at the LHC". In: *Physics Letters B* 716.1 (2012), pp. 30–61.

[13] The ATLAS Collaboration. "Observation of a new particle in the search for the Higgs boson at the LHC". In: *Physics Letters B* 716.1 (2012), pp. 1–29.

[14] The ATALS Collaboration. "Combined Measurement of the Higgs Boson Mass from the $H \to \gamma\gamma$ and $H \to ZZ^* \to 4\ell$ Decay Channels with the ATLAS Detector Using $\sqrt{s} =$ 7, 8, and 13 TeV pp Collision Data". In: *Phys. Rev. Lett.* 131 (25 2023), p. 251802.

[15] Fangyi Guo et al. "Expected measurement precision of the branching ratio of the Higgs boson decaying to the di-photon at the CEPC". In: *Chinese Physics C* 47.4 (2023), p. 043002.

[16] Akimasa Ishikawa. "Search for invisible decays of the Higgs boson at the ILC". In: (2019).

[17] J. de Blas et al. "Higgs Boson studies at future particle colliders". In: *Journal of High Energy Physics* 2020.1 (2020), p. 139. ISSN: 1029-8479.

[18] Yuhang Tan et al. "Search for invisible decays of the Higgs boson produced at the CEPC *". In: *Chinese Physics C* 44.12 (2020), p. 123001.

[19] S. L. Glashow. "Partial Symmetries of Weak Interactions". In: *Nucl. Phys.* 22 (1961), pp. 579 –588.

[20] S. Weinberg. "A Model of Leptons". In: *Phys. Rev. Lett.* 19 (1967), pp. 1264 –1266.

[21] J. R. Ellis, J. L. Lopez, and D. V. Nanopoulos. "Supersymmetry, supergravity and R(b) revisited in the light of LEP - 2". In: *Phys. Lett. B* 397 (1997), pp. 88 –93.

[22] M. I. Vysotsky et al. "Electroweak radiative corrections in Z boson decays". In: *Phys. Usp.* 39 (1996), pp. 503 –538.

[23] M. et al. Acciarri. "Measurement of R(b) and Br(b $\to$ lepton neutrino X) at LEP using double tag methods". In: *Eur. Phys. J. C* 13 (2000), pp. 47 –61.

[24] G. et al. Abbiendi. "A Measurement of R(b) using a double tagging method". In: *Eur. Phys. J. C* 8 (1999), pp. 217 –239.

[25] P. et al. Abreu. "A Precise measurement of the partial decay width ratio R(b)**0 = Gamma(b antib) / Gamma(had)". In: *Eur. Phys. J. C* 10 (1999), pp. 415 –442.

[26] R. et al. Barate. "A Measurement of R(b) using mutually exclusive tags". In: *Phys. Lett. B* 401 (1997), pp. 163 –175.

[27] K. et al. Abe. "Measurement of the branching ratio of the Z0 into heavy quarks". In: *Phys. Rev. D* 71 (2005), p. 112004.

[28] S. et al. Schael. "Precision electroweak measurements on the Z resonance". In: *Phys. Rept.* 427 (2006), pp. 257 –454.

[29] CEPC Study Group. "CEPC Conceptual Design Report: Volume 2 - Physics & Detector". In: (2018).

[30] A. et al. Abada. "FCC-ee: The Lepton Collider: Future Circular Collider Conceptual Design Report Volume 2". In: *Eur. Phys. J. ST* 228.2 (2019), pp. 261 –623.

[31] B. Li et al. "Performance study of the relative decay width measurement in hadronic decays of Z boson at CEPC by using the template method". In: *Int. J. Mod. Phys. A* 36.27 (2021), p. 2150207.

[32] Xiaocong Ai et al. "Flavor Physics at CEPC: a General Perspective". In: (Dec. 2024).

[33] Roel Aaij et al. "Observation of CP Violation in Charm Decays". In: *Phys. Rev. Lett.* 122.21 (2019), p. 211803.

[34] Roel Aaij et al. “Measurements of prompt charm production cross-sections in pp collisions at $\sqrt{s} = 13$ TeV”. In: *JHEP* 03 (2016). [Erratum: JHEP 09, 013 (2016), Erratum: JHEP 05, 074 (2017)], p. 159.

[35] Roel Aaij et al. “Search for time-dependent CP violation in $D^0 \to K^+K^-$ and $D^0 \to \pi^+\pi^-$ decays”. In: *Phys. Rev. D* 104.7 (2021), p. 072010.

[36] R. Aaij et al. “Search for CP violation in the phase space of $D^0 \to \pi^-\pi^+\pi^0$ decays with the energy test”. In: *JHEP* 09 (2023). [Erratum: JHEP 04, 040 (2024)], p. 129.

[37] CDF and D0 Collaborations. “Combination of CDF and D0 results on the mass of the top quark using up $9.7\ \mathrm{fb}^{-1}$ at the Tevatron”. In: (Aug. 2016).

[38] ATLAS Collaboration. “Measurement of the top quark mass in the $t\bar{t} \to$ lepton+jets channel from $\sqrt{s} = 8$ TeV ATLAS data and combination with previous results”. In: *Eur. Phys. J. C* 79.4 (2019), p. 290.

[39] CMS Collaboration. “Measurement of the top quark mass using proton-proton data at $\sqrt{(s)}$ = 7 and 8 TeV”. In: *Phys. Rev. D* 93.7 (2016), p. 072004.

[40] Armen Tumasyan et al. “Measurement of the top quark mass using a profile likelihood approach with the lepton + jets final states in proton–proton collisions at $\sqrt{s} = 13\,\mathrm{TeV}$”. In: *Eur. Phys. J. C* 83.10 (2023), p. 963.

[41] Manel Martinez and Ramon Miquel. “Multiparameter fits to the t anti-t threshold observables at a future e+ e- linear collider”. In: *Eur. Phys. J. C* 27 (2003), pp. 49–55.

[42] Katja Seidel et al. “Top quark mass measurements at and above threshold at CLIC”. In: *Eur. Phys. J. C* 73.8 (2013), p. 2530.

[43] Tomohiro Horiguchi et al. “Study of top quark pair production near threshold at the ILC”. In: (Oct. 2013).

[44] H. Abramowicz et al. “Top-Quark Physics at the CLIC Electron-Positron Linear Collider”. In: *JHEP* 11 (2019), p. 003.

[45] A. Abada et al. “FCC-ee: The Lepton Collider: Future Circular Collider Conceptual Design Report Volume 2”. In: *Eur. Phys. J. ST* 228.2 (2019), pp. 261–623.

[46] Zhan Li et al. “Top quark mass measurements at the $t\bar{t}$ threshold with CEPC”. In: *Eur. Phys. J. C* 83.4 (2023). [Erratum: Eur.Phys.J.C 83, 501 (2023)], p. 269.

[47] Maximilian Stahlhofen and Andre Hoang. “NNLL top-antitop production at threshold”. In: *PoS* RADCOR2011 (2011), p. 025.

[48] André H. Hoang and Maximilian Stahlhofen. “The Top-Antitop Threshold at the ILC: NNLL QCD Uncertainties”. In: *JHEP* 05 (2014), p. 121.

[49] R. Assmann et al. “Calibration of centre-of-mass energies at LEP 2 for a precise measurement of the W boson mass”. In: *Eur. Phys. J. C* 39 (2005), pp. 253–292.

[50] G. Abbiendi et al. “Determination of the LEP beam energy using radiative fermion-pair events”. In: *Phys. Lett. B* 604 (2004), pp. 31–47.

[51] S. Boogert et al. “Polarimeters and Energy Spectrometers for the ILC Beam Delivery System”. In: *JINST* 4 (2009), P10015.

[52] Yulei Zhang et al. “Search for Long-lived Particles at Future Lepton Colliders Using Deep Learning Techniques”. In: (June 2025).

[53] Jiarong Yuan, Huajie Cheng, and Xuai Zhuang. “Prospects for slepton pair production in the future e^-e^+ Higgs factories”. In: (Mar. 2022).

[54] Glen Cowan. *Discovery sensitivity for a counting experiment with background uncertainty*. `http://www.pp.rhul.ac.uk/~cowan/stat/medsig/medsigNote.pdf`, retrieved 9th April 2021.

[55] I. Smiljanic, I. Bozovic, and G. Kacarevic. “Metrological Uncertainties in the Integrated Luminosity Measurement with the Updated Design of a Detector at CEPC”. In: *PTEP* 2024.10 (2024), 103H02.

[56] I. Bozovic Jelisavcic, I. Smiljanic, and G. Kacarevic. “Electromagnetic deflection of the initial state at the Z-pole at CEPC”. EU Edition of the CEPC Workshop, University of Edinburgh. July, 2023.

[57] G. Voutsinas et al. “Beam-beam effects on the luminosity measurement at LEP and the number of light neutrino species”. In: *Physics Letters B* 800 (2020), p. 135068.

[58] I. Smiljanic et al. “Systematic uncertainties in integrated luminosity measurement at CEPC”. In: *Journal of Instrumentation* 17.9 (2022), P09014.

[59] Carlo M. Carloni Calame et al. “Electroweak corrections to $e^+e^- \to \gamma\gamma$ as a luminosity process at FCC-ee”. In: *Phys. Lett. B* 798 (2019), p. 134976.

[60] G. Balossini et al. “Photon pair production at flavour factories with per mille accuracy”. In: *Physics Letters B* 663.3 (2008), pp. 209–213. ISSN: 0370-2693.

[61] The ALEPH Collaboration et al. “Electroweak measurements in electron–positron collisions at W-boson-pair energies at LEP”. In: *Physics Reports* 532.4 (2013). Electroweak Measurements in Electron-Positron Collisions at W-Boson-Pair Energies at LEP, pp. 119–244. ISSN: 0370-1573.

[62] The OPAL Collaboration and G. Abbiendi et al. “Multi-photon production in ee collisions at $\sqrt{s}$ =181-209 GeV”. In: *Eur.Phys.J. C* 26.1 (2003). Electroweak Measurements in Electron-Positron Collisions at W-Boson-Pair Energies at LEP, pp. 331–344. ISSN: 1434-6052.

[63] Jie Gao. “CEPC Technical Design Report: Accelerator”. In: *Radiation Detection Technology and Methods* 8 (2024), pp. 1–1105.

[64] Alain Blondel et al. “Polarization and Centre-of-mass Energy Calibration at FCC-ee”. In: (Sept. 2019).

[65] Jack Heron. *Update of availability studies*. presented at the FCC-ee ATDC 16 availability and operation model meeting, 23 January 2025.